

Peer review status:

This is a non-peer-reviewed preprint submitted to EarthArXiv. The manuscript has been submitted for publication in Nature Water.

Global assessment of terrestrial water cycle	001
resilience	002
	003
	004
	005
	006
	007
	008
	009
Romi A. Lotcheris ^{1,2*} , Nielja S. Knecht ^{1,2} ,	010
Lan Wang-Erlandsson ^{1,2,3} , Juan C. Rocha ^{1,2*}	011
¹ *Stockholm Resilience Centre, Stockholm University, Stockholm,	012
SE-106 91, Sweden.	013
² Bolin Centre for Climate Research, Stockholm University, Stockholm,	014
10587, Sweden.	015
³ Potsdam Institute for Climate Impact Research, Member of the	016
Leibnitz Associations, Potsdam, 14473, Germany.	017
*Corresponding author(s). E-mail(s): romi.lotcheris@su.se ;	018
juan.rocha@su.se ;	019
	020
	021
	022
	023
	024
	025
	026
	027
	028
	029
	030
	031
	032
	033
	034
	035
	036
	037
	038
	039
	040
	041
	042
	043
	044
	045
	046

047 **1 Introduction**

048

049 Water plays a crucial role in regulating the functioning and stability of the Earth sys-
050 tem [1–3]. Yet, research points to widespread anthropogenic pressures on the terrestrial
051 water cycle [3–5]. Green water - the water which is available to and used by vege-
052 tation - is critical for maintaining hydro-ecological and hydro-climatic Earth system
053 functions [1, 2, 6], mediating soil–water–vegetation interactions that generate critical
054 feedbacks for ecosystem and climate functioning. These feedbacks depend strongly on
055 hydro-ecological context. For example, in energy-limited tropical forests, transpira-
056 tion is closely linked to moisture recycling dynamics that are affected by land cover
057 change [7, 8], whereas in water-limited ecosystems, soil moisture-vegetation feedbacks
058 play a more important role [9, 10]. Through these feedbacks, changes to green water
059 variables can have self-amplifying, non-linear effects [3].

060

061 Given the potential for these feedbacks to generate non-linear changes in the water
062 cycle and vegetation dynamics, understanding green water resilience is critical for
063 assessing how human pressures are altering the water cycle. Resilience describes a sys-
064 tem’s ability to absorb disturbances, reorganize, and maintain its essential structure
065 and functions [11–13]. As a system loses resilience, it becomes vulnerable to abrupt
066 transitions from one qualitative regime to another [14]. Early warning signals (EWS)
067 have been used as statistical proxies for resilience. Often based on measured changes
068 to autocorrelation and variance [12, 15], EWS have been used to assess resilience in
069 terrestrial ecosystems, applied to gross primary productivity and leaf area index [16],
070 normalized difference vegetation index [17–19], or vegetation optical depth [17, 20].
071 Despite the close coupling of green water variables to terrestrial ecosystems, water is
072 typically treated as a static explanatory driver, thereby not accounting for changes
073 in the water cycle dynamics that both drive and respond to changes in vegetation.
074 As a result, the resilience of green water variables themselves is not yet well under-
075 stood. Additionally, ground-truth validation of vegetation resilience assessments has
076

077

been done in only a few documented, often local cases (see ref. [21]). A validation of green water resilience indicators against ground-truth observations has not yet been undertaken.	093
	094
	095
	096
	097
	098
	099
	100
	101
	102
	103
	104
	105
	106
	107
	108
	109
	110
	111
	112
	113
	114
	115
	116
	117
	118
	119
	120
	121
	122
	123
	124
	125
	126
	127
	128
	129
	130
	131
	132
	133
	134
	135
	136
	137
	138

139 **Table 1** Early-warning signals (EWS) used in this study, the indicators used for each EWS and
 140 their typical signs, and their interpretation. Indicators are computed in 5-year rolling windows and
 141 summarised by Kendall's τ trend statistic.

142	143	EWS	Indicator	Shorthand	Interpretation
144	145	Critical Slowing Down (CSD)	\uparrow Lag-1 autocorrelation	AC1 (τ_{AC1})	Trend in short-term persistence
146	147		\uparrow Standard deviation	SD (τ_{SD})	Trend in variability
148	149	<i>Increased tendency for system states to be distributed further from equilibrium and slower to recover. A wider and shallower basin of attraction reduces resilience</i>			
151	152	Critical Speeding Up (CSU)	\downarrow Lag-1 autocorrelation	AC1 (τ_{AC1})	Trend in short-term persistence
153	154		\downarrow Standard deviation	SD (τ_{SD})	Trend in variability
155	156	<i>Narrowing of the basin of attraction increases the likelihood of exiting the basin. Resilience reduced by increasing vulnerability to stochastic transitions.</i>			
158	159	Flickering	$\uparrow \downarrow$ Skewness	Skew (τ_{Skew})	Trend in asymmetry
160			\uparrow Kurtosis	Kurt (τ_{Kurt})	Trend in tail-heaviness
161	162	<i>Increasing tendency for system states to exist at distribution tails (i.e., more frequent/extreme excursions).</i>			
163	164	Fractal dimension	\downarrow Fractal dimension	FD (τ_{FD})	Trend in temporal structure & long-term memory
166	167	<i>Scale-free measure of temporal memory of a time series. Increasing self-similarity and slower recovery reduces resilience.</i>			

169
 170
 171 series without detected breakpoints) (Section 4.3). We use these in a machine-learning
 172 framework to evaluate how well EWS anticipate changes in green water variables, and
 173 understand which indicators and directions are informative (Section 4.4).

174 We apply this approach to precipitation, transpiration, and soil moisture, representing the input, storage, and release of water available to terrestrial vegetation.
 175 Because the three variables are derived from distinct satellite products with different noise characteristics, uncertainties, and spatial coverage, we estimate EWS and
 176 interpret results separately for each variable.
 177

2.1 Abrupt shifts in green water are coherent in time and space	185
	186
We detect abrupt shifts in all three green water variables, with pronounced spatial and temporal coherence in breakpoint timing (Fig. 6). Neighbouring pixels frequently shift in the same years, indicating synchronous changes across larger land areas. The affected land area also accumulates over time. Between 2000 and 2020, 22.6% of land between 60°S and 60°N has experienced an abrupt shift in precipitation, 7.5% in transpiration, and 3.5% of land area excluding dense tropical forests has experienced abrupt shifts in soil moisture (Supplementary Fig. 7).	187
	188
	189
	190
	191
	192
	193
	194
	195
	196
	197
	198
	199
	200
	201
	202
	203
	204
	205
	206
	207
	208
	209
	210
	211
	212
	213
	214
	215
	216
	217
	218
	219
	220
	221
	222
	223
	224
	225
	226
	227
	228
	229
	230
Transpiration. Abrupt shifts are generally detected in the northern high-latitudes, South America, Central Asia, and Australia, with almost none detected in temperate ecosystems (Fig. 6a). Abrupt shifts in the high-latitudes are associated with an increase in transpiration, whereas shifts South America, Central Asia, and Australia are generally associated with a decrease. In the tropics, high absolute differences, and lower proportional change is likely the result of higher baseline transpiration. The opposite effect occurs in drier regions, where higher absolute differences also lead to greater proportional changes (Fig. 6b). We also find an increase in transpiration in the Sahel region following abrupt shifts, with breakpoints detected in the 2010s.	199
	200
	201
	202
	203
	204
	205
	206
	207
	208
	209
	210
	211
	212
	213
	214
	215
	216
	217
	218
	219
	220
	221
	222
	223
	224
	225
	226
	227
	228
	229
	230
Soil moisture. Abrupt shifts are more common in more arid regions, with a smaller absolute decrease in soil moisture following an abrupt shift compared to transpiration and precipitation (Figure 6a and b). Large parts of Argentina and southern Brazil show shifts in the early 2000s, which are followed by substantial proportional declines in soil moisture. Adjacent regions show shifts in the later 2000s and 2010s. Southern Africa, western Australia, and northern Mexico show similar patterns. Shifts associated with increases in soil moisture are detected in the Sahel region, progressing northwards in later years. We also detect increasing soil moisture following abrupt shifts in Eastern China and Eastern Australia.	214
	215
	216
	217
	218
	219
	220
	221
	222
	223
	224
	225
	226
	227
	228
	229
	230

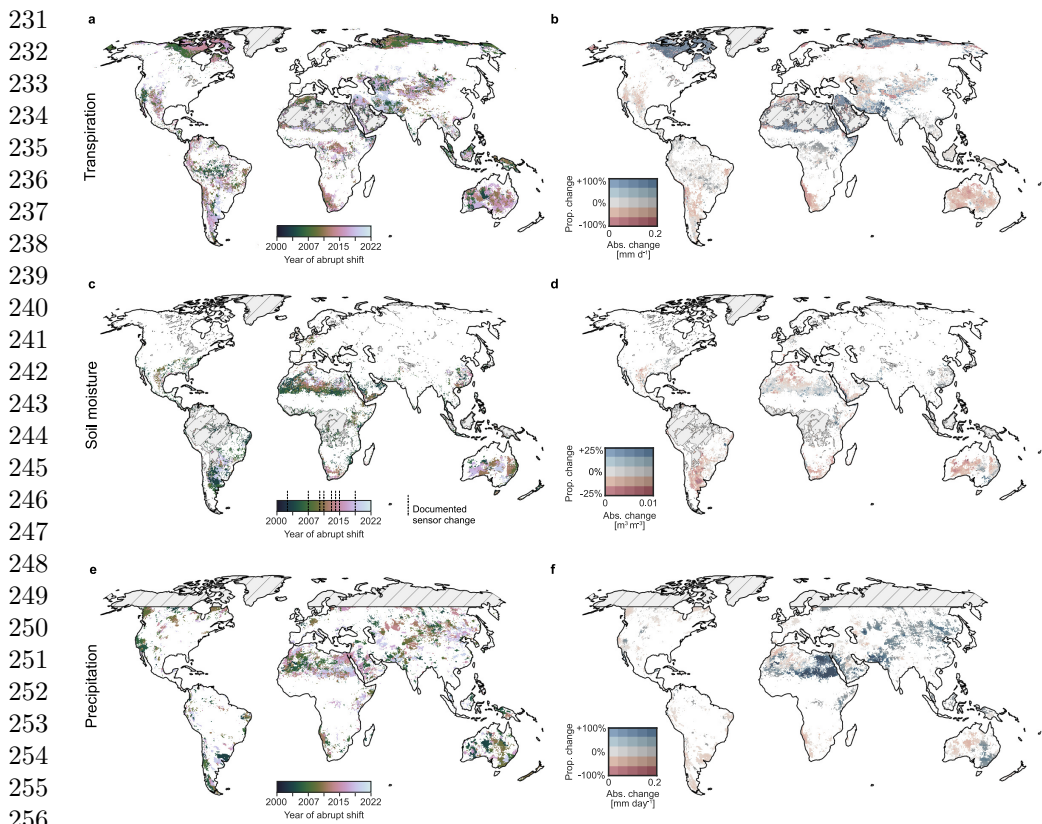


Fig. 1 Spatial patterns of abrupt shift in mean for green water variables. Year of first detected significant breakpoint from the structural change test ($p < 0.05$), and the proportional and absolute difference between the mean before and after the detected breakpoint in transpiration (a - b), soil moisture (c - d) and precipitation (e - f). The proportion of change is calculated by dividing the mean after the breakpoint by the mean before the breakpoint. Darker colours indicate both a high proportional change and a high absolute difference in mean before and after the breakpoint. Lighter colours indicate a high proportional change, but a low absolute difference. No data is given by a grey hatch.

265 **Precipitation.** Abrupt shifts are concentrated in the mid-latitudes (approxi-
266 mately between 30°N and 30°S), with no shifts detected in humid equatorial regions.
267 Shifts associated with an increase in precipitation are concentrated in central and
268 eastern Asia and northern Africa, while those associated with a decrease are found
269 in South America, southern Africa, and Australia (Figure 6c). We detect fewer shifts
270 in South America compared to soil moisture and transpiration, while southern Africa
271
272
273
274
275
276

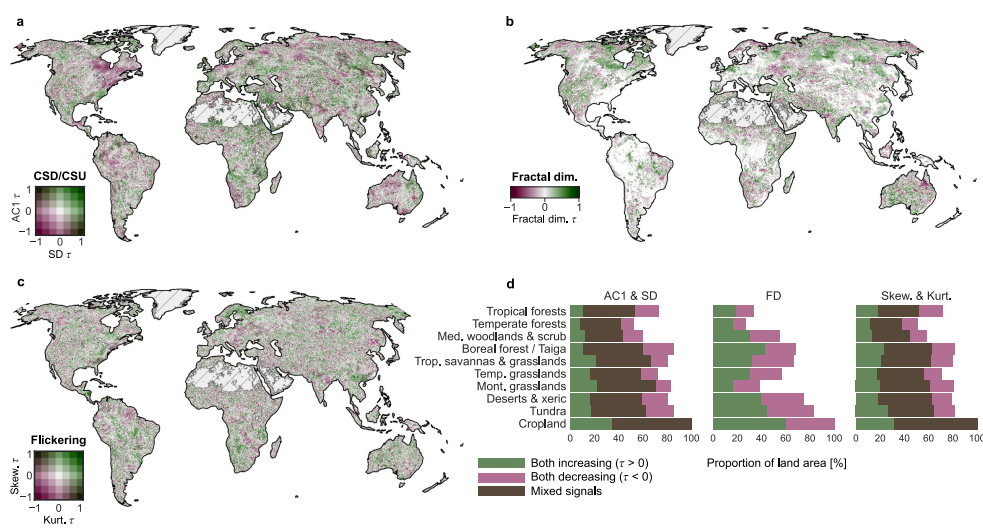
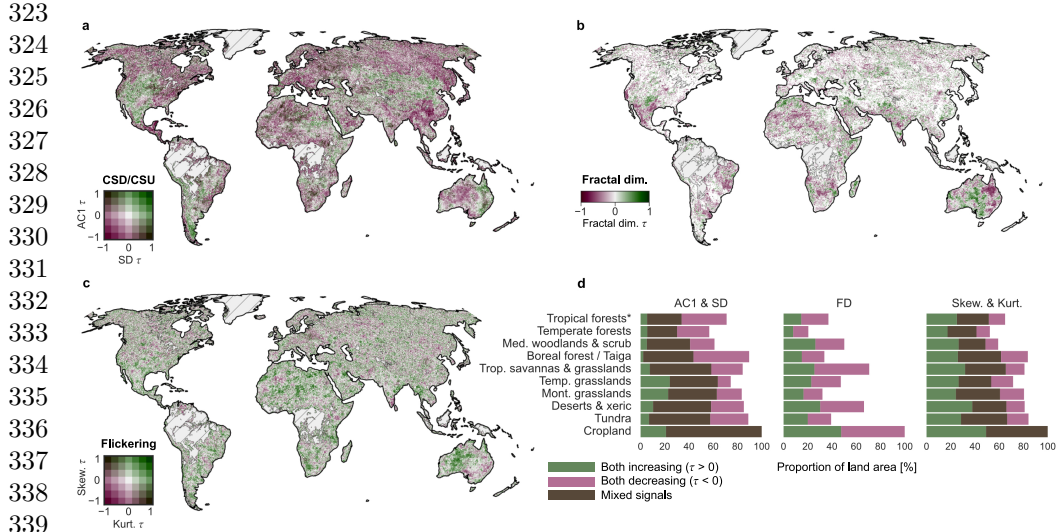


Fig. 2 Spatial patterns of early warning signals (EWS) for transpiration. Panels (a - c): (a) Spatial patterns of changes to autocorrelation (AC1) and standard deviation (SD), related to critical slowing down (CSD) and critical speeding up (CSU); (b) Spatial patterns of changes to the fractal dimension, where decreasing FD is the EWS; (c) Spatial patterns of changes to skewness and kurtosis, related to flickering. Green shading denotes pixels where both metrics are simultaneously increasing, pink shading denotes pixels where both are decreasing; brown shading denotes pixels where one metric increases while the other decreases. White regions did not exhibit statistically significant trends in the respective metrics, grey hatch indicates regions with missing data. All trends were assessed via Kendall's τ ($p < 0.05$). Bar plots show the proportion of land area for each EWS where indicators are simultaneously increasing, decreasing, or showing mixed signals.

shows synchronous shifts around the 2010s. Both regions experienced abrupt declines in precipitation.

2.2 Resilience loss in green water globally

Signals of resilience loss in the terrestrial water cycle occurred across all biome types (Figs. 2–4). Spatial patterns are largely heterogenous, but some regional patterns emerge, which differ across green water variables (transpiration, soil moisture, precipitation) and EWS types (Section 4.2). CSD is more frequent in water-limited systems, especially grasslands and drylands, while higher-latitude ecosystems show more flickering and CSU. Tropical and temperate grassland biomes consistently exhibit higher proportions of EWS across variables, particularly signals of CSD and FD.



341 **Fig. 3 Spatial patterns of early warning signals (EWS) for soil moisture.** Panels (a - c): (a)
342 Spatial patterns of changes to autocorrelation (AC1) and standard deviation (SD), related to critical
343 slowing down (CSD) and critical speeding up (CSU); (b) Spatial patterns of changes to the fractal
344 dimension (FD), where decreasing FD is the EWS; (c) Spatial patterns of changes to skewness and
345 kurtosis, related to flickering. Green shading denotes pixels where both metrics are simultaneously
346 increasing, pink shading denotes pixels where both are decreasing; brown shading denotes pixels where
347 one metric increases while the other decreases. White regions did not exhibit statistically significant
348 trends in the respective metrics, grey hatch indicates regions with missing data. All trends were
349 assessed via Kendall's τ ($p < 0.05$). Asterisk marks biomes where satellite coverage of soil moisture
350 is incomplete; proportions reflect only pixels within the biome where data was available.

350 **Transpiration.** While mixed AC1-SD signals dominate across biomes (Figure 2a),
351 CSD signals show prominent clusters in dryland and savanna regions in southern South
352 America, the Miombo woodlands in Southern Africa, the Sahel, and north-eastern
353 Australia (Fig. 2a and d). CSU signals are most prevalent in boreal forests, tundra, and
354 deserts. FD decreases in tundra, deserts, tropical grasslands, and temperate grasslands
355 biomes (Fig. 2d). Flickering is most frequent in mid- to high latitudes, with high
356 proportions in tundra and boreal forests, but also tropical savannas, including Brazil
357 (Fig. 2c).

358 **Soil moisture.** CSD-based EWS are less frequent, also dominated by mixed
359 AC1-SD signals (Fig. 3a). Some CSD clusters were present in southern North Amer-
360 ica, the Andes and southern Argentina, north-eastern Australia, and central Asia, with
361

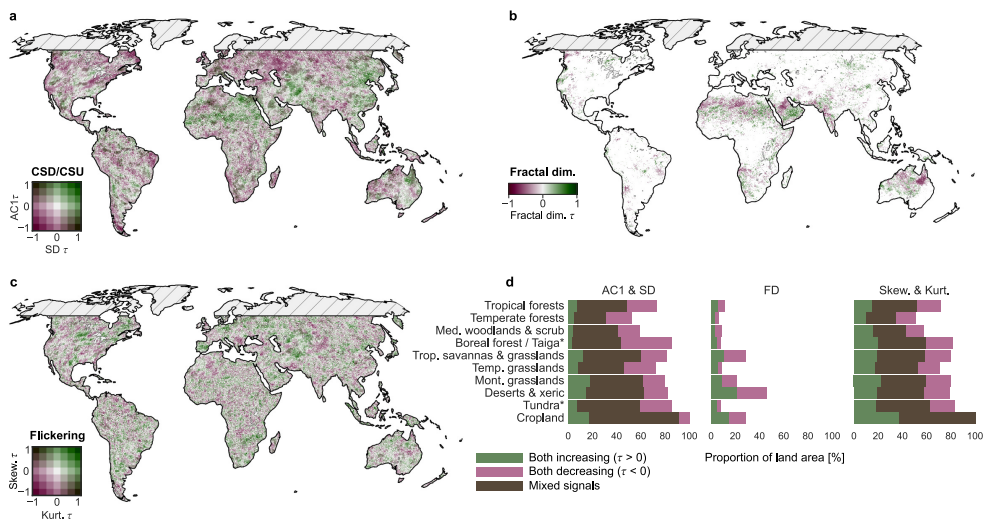


Fig. 4 Spatial patterns of early warning signals (EWS) for precipitation. Panels (a - c): (a) Spatial patterns of changes to autocorrelation (AC1) and standard deviation (SD), related to critical slowing down (CSD) and critical speeding up (CSU); (b) Spatial patterns of changes to the fractal dimension, where decreasing FD is the EWS; (c) Spatial patterns of changes to skewness and kurtosis, related to flickering. Green shading denotes pixels where both metrics are simultaneously increasing, pink shading denotes pixels where both are decreasing; brown shading denotes pixels where one metric increases while the other decreases. White regions did not exhibit statistically significant trends in the respective metrics, grey hatch indicates regions with missing data. All trends were assessed via Kendall's τ ($p < 0.05$). Bar plots show the proportion of land area. Asterisk marks biomes where satellite coverage of precipitation is incomplete; proportions reflect only pixels within the biome where data was available.

highest proportions in temperate and montane grasslands (Fig. 3d). Spatial overlap between soil moisture and transpiration CSD occurs in parts of Argentina, southern Brazil, and central Mexico (Figs. 2a and 3a). CSU signals in soil moisture are most frequent in boreal forests and tundras. FD decreases in subtropical and dryland regions, tropical grasslands, deserts, as well as temperate grasslands and Mediterranean forests (Fig. 3b). Flickering signals were heterogenous, with less clear spatial patterns.

Precipitation. Mixed AC1-SD signals dominated across biomes (Fig. 4a). CSD was most prevalent in subtropical and arid regions, with deserts and tropical grasslands showing the highest proportions. CSU signals were more common in temperate grasslands and forests, and in tropical savannas (Fig. 4d). Tropical forests, which show

369
370
371
372
373
374
375
376
377
378
379
380
381
382
383
384
385
386
387
388
389
390
391
392
393
394
395
396
397
398
399
400
401
402
403
404
405
406
407
408
409
410
411
412
413
414

415 few CSD signals, exhibit relatively more CSU for both transpiration and precipitation.
416
417 FD decreases in precipitation are rare compared to transpiration and soil moisture but,
418 where present, are concentrated in subtropical drylands, especially deserts and tropi-
419 cal savannas (Fig. 4b). Flickering patterns are heterogeneous, with highest proportions
420 in montane and tropical grasslands (Fig. 4c).
421
422

423 Our results are robust across different methods to assess the direction and sig-
424
425 nificance of the EWS (Supplementary Fig. 6). While sensitive to the rolling window
426 length and temporal aggregation, we find that a 5-year rolling window at weekly time-
427 scales best balances noise and excessive dampening of longer windows (section 4.5;
428
429 Supplementary Table 1).
430
431
432

433 **2.3 Performance and EWS are context dependent**

434

435 To understand under which conditions early-warning signals (EWS) can anticipate
436 abrupt shifts in green water dynamics, we use a machine learning framework (Section
437 4.4) to test how much both EWS and environmental variables contribute to predicting
438 detected abrupt shifts (Section 2.1). We use Shapley (SHAP) values, reported as log-
439 odds, to quantify the marginal contribution of EWS and environmental variables to
440 predicting abrupt shifts that occurred at least 12 years after the start of the time
441 series. EWS predictors are computed only from observations prior to the detected
442 shift; environmental predictors summarise conditions over the full time series. Positive
443 SHAP values indicate that explanatory variables raise the probability of detecting a
444 True abrupt shift, whereas negative values indicate higher chances of False shifts. We
445 find EWS make only a modest contribution to model skill; most predictive power comes
446 from environmental context. However, the relative importance of EWS compared to
447 environmental variables differs across hydro-ecological system types and green water
448 variables (Fig. 5).
449
450
451
452
453
454
455
456
457
458
459
460

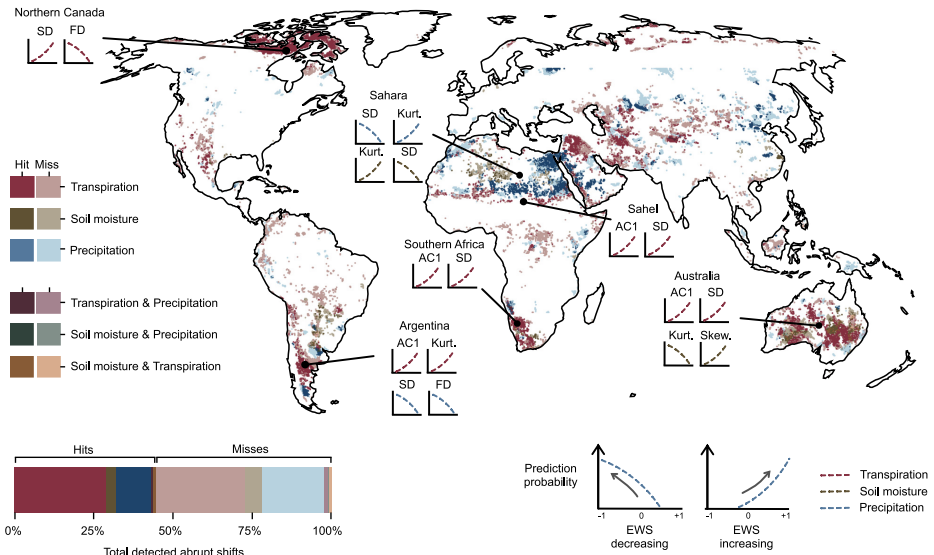


Fig. 5 Different regions and green water variables are characterised by different EWS τ as the strongest predictors of abrupt shifts. For transpiration, soil moisture, precipitation, and their combinations, regional summaries list the two most influential EWS τ (SHAP-ranked) and the sign associated with increased predicted probability of an abrupt shift; both increasing and decreasing EWS τ can be associated with higher risk, illustrated in the bottom right schematic. Spatial shading indicates hits (darker) and misses (lighter). The bottom bar plot summarises their respective proportions for the green water variables and their combinations.

Transpiration. Models achieve the highest skill for transpiration (PR AUC = 0.49 versus baseline 0.06; Supplementary Table 10). Environmental variables account for most of this skill, with EWS adding some complementary information. Gross primary productivity variance, autocorrelation (τ_{AC1}), transpiration variance, and PET variance are dominant predictors (Fig. A1a). Correctly predicted shifts cluster in Northern Canada, southern South America, Southern Africa, the Sahel, and Australia (Figure 5). In these regions, most influential EWS combinations typically involved increasing τ_{AC1} and τ_{SD} , which are associated with higher predicted probability of an abrupt shift. This is consistent with CSD in dryland and transition zones (Section 2.2). Missed shifts, together with regional SHAP summaries, suggest that EWS for transpiration have limited predictive value in humid tropical forests and some temperate regions (Fig. A1).

461
462
463
464
465
466
467
468
469
470
471
472
473
474
475
476
477
478
479
480
481
482
483
484
485
486
487
488
489
490
491
492
493
494
495
496
497
498
499
500
501
502
503
504
505
506

507 **Soil moisture.** Models achieve only modest skill (PR AUC ≈ 0.21 versus baseline
508 0.02; Supplementary Table 10). Abrupt shifts are rarer and spatially isolated, and envi-
509 ronmental and climatic variables dominate model performance. Mean temperature,
510 soil moisture variance, temperature variance, temperature trend, and PET variance
511 are dominant predictors (Fig. A1b). Detected soil moisture shifts occur mainly in
512 parts of Australia and the Sahara, where combinations of τ_{Kurt} , τ_{Skew} , and τ_{SD} were
513 important (Fig. 5). However, EWS τ do not exhibit clear, consistent associations with
514 increased predicted probability (Fig. A2b), indicating that the indicators used here
515 provide little systematically predictive information for soil moisture at the global scale.
516

517 **Precipitation.** Model performance for precipitation is intermediate (PR AUC
518 = 0.33 versus baseline 0.05; Supplementary Table 10). Environmental drivers again
519 explain most predictive power (Drivers-only PR AUC = 0.24; EWS-only PR AUC
520 = 0.06), but EWS add complementary information in the full model (PR AUC =
521 0.33) τ_{Kurt} , τ_{SD} , temperature variance, mean precipitation were are dominant envi-
522 ronmental predictors (Fig. A1c). Correctly predicted abrupt shifts in precipitation
523 are concentrated along dryland boundaries, including Egypt and regions north of the
524 Sahel, with additional clusters in Argentina and parts of south-eastern Russia and
525 China (Fig. 5). In Argentina, decreasing τ_{SD} and τ_{FD} are associated with higher
526 predicted probability, whereas in the Sahara and northern Sahel decreasing τ_{SD} and
527 increasing τ_{Kurt} is influential. These patterns are consistent with critical speeding up
528 of precipitation in drier margins of humid systems (Section 2.2). Increasing kurto-
529 sis, and decreasing SD and FD τ show linear associations with increased predicted
530 probability (Fig. A2), consistent with CSU-like signals having some predictive value,
531 particularly for more humid systems (Fig. A1).

532
533
534
535
536
537
538
539
540
541
542
543
544
545
546
547
548
549
550
551
552

3 Discussion 553

We find ecosystem-dependent signatures of resilience loss in green water variables. For 554 transpiration, we find that increasing AC1 and SD provide predictive power in estimating 555 abrupt shifts. Signals of CSD (simultaneously increasing AC1 and variance) 556 and decreasing FD were most pronounced in drylands and transitional systems, 557 consistent with evidence of lower resilience with increasing aridity [27], and with research 558 identifying the regions such as the Caatinga, prairies, and grasslands of North America 559 and Asia as sensitive to water availability [28]. Regions where we detect CSD in 560 transpiration and soil moisture overlap with regions identified as at risk of abrupt 561 aridification [10, 29, 30]. Crucially, signals of resilience loss in drylands, grasslands, 562 and tropical forests point towards potential risks to green water functions that may 563 disproportionately affect communities in the Global South. 564

For precipitation, decreases in SD and FD and increases in kurtosis were associated 565 with a higher probability of detecting an abrupt shift. Previous studies in the Amazon 566 have reported increasing AC1 and variance in vegetation, interpreting decreasing 567 AC1 and variance in wetter regions as resilience gain [17, 20, 31]. We do not detect 568 widespread CSD-like EWS in Amazon precipitation, suggesting that observed vegetation 569 resilience loss is unlikely to be explained solely by CSD in a precipitation driver 570 [15], and may instead be consistent with resilience loss in vegetation. We find that 571 CSU-like signals in precipitation are associated with an increased probability of abrupt 572 shifts, particularly in drier, water-limited regions such as savannas and temperate 573 grasslands. 574

In boreal forest and tundra biomes, signals of CSU were prevalent across all green 575 water variables. In these regions, rapid warming has led to permafrost thaw and 576 improved soil drainage [32], earlier snow melt [33], and vegetation reorganisation, for 577 example an increase in deciduous vegetation in boreal forests with changes in phe- 578 nology and a faster growing period and shrub encroachment in the tundra [34, 35]. 579

599 The effects these changes have on soil moisture and vegetation may contribute to
600 CSU signals in transpiration. Previous research has similarly found decreasing AC1 in
601 the enhanced vegetation index in tundra regions in North America [36]. Additionally,
602 signals of flickering in transpiration may reflect more frequent excursions into alterna-
603 tive regimes (e.g., snow vs. rain, frozen vs. thawed) brought on by increasing global
604 temperatures [33].
605

606 We present a methodological approach to understand the extent to which EWS are
607 useful in predicting abrupt shifts. We find limited, but non-negligible, added value of
608 using EWS when predicting abrupt shifts, and demonstrate that including only CSD
609 as a leading indicator of critical transitions may be misleading. Ecosystems themselves
610 differ in their soil–water–vegetation coupling dynamics, water availability adaptation
611 strategies, plant-stress regimes, and the temporal scales of dominant forcing variables.
612

613 For these reasons, a single EWS is likely to be insufficient. Instead, we find a wider
614 portfolio of context appropriate EWS may be warranted. The differences in the rel-
615 ative importance of some EWS compared to other indicators across aridity classes
616 also suggest that the predictive power of EWS depends on climatic and ecosystem
617 characteristics. This is critical for understanding where one might expect EWS to be
618 informative. While we find EWS may not be broadly powerful predictors on their own,
619 they could provide important information when combined with environmental con-
620 text and a plausible understanding of where a signal may be ecologically informative.
621 We also highlight that resilience assessments may benefit from accounting for these
622 potential multiple pathways by adopting a multiple indicator approach.
623

624 By focusing on non-linear changes to green water variables, we provide a comple-
625 mentary perspective to previous research on related aspects of water resilience [5, 37].
626 Non-linear responses are expected when a state variable’s response to a forcing is nei-
627 ther gradual nor proportional to the magnitude of the disturbance, consistent with
628 threshold and feedback-related processes in the water cycle [38–42].
629

Our findings add an important empirical perspective on the global stability of key water cycle components, and we further identify several avenues for future research. Integrating analysis from direct measurements and ground networks (e.g., flux tower measurements, in-situ soil moisture) could help to better resolve spatial heterogeneity that coarse satellite products cannot capture. CSD theory presumes a slow approach to a single driver-induced bifurcation, whereas terrestrial systems are typically subject to interacting and evolving drivers [43, 44], for example, projected changes in the strength and spatial pattern of climate oscillations [45, 46]. We show that including information on drivers improves the ability of EWS to predict abrupt shifts. Improved understanding of the local, distal, and interacting temporal and spatial influence of these drivers, can further inform long-term ecosystem management strategies, and contribute to safeguarding water as a critical stabilising force in the Earth system.

645
646
647
648
649
650
651
652
653
654
655
656
657
658
659
660
661
662
663
664
665
666
667
668
669
670
671
672
673
674
675
676
677
678
679
680
681
682
683
684
685
686
687
688
689
690

691 from PERSIANN-CDR (Precipitation Estimation from Remotely Sensed Information
692 using Artificial Neural Networks - Climate Data Record, 0.25° , 1983 - present, with a
693 coverage of 60°S to 60°N) [51].
695

696 Single-sensor remote sensing time series are preferred in EWS assessments of
697 resilience loss. For soil moisture, where long, single-sensor time series were not avail-
698 able, we used remotely sensed data that have been structurally corrected for changes
700 to autocorrelation and variance in the merging procedure (ESA CCI SM) [50]. For
702 precipitation, PERSIANN-CDR does not use cumulative distribution function match-
704 ing for time series merging, or require posteriori distribution or bias correction [52],
705 as this is handled directly by the neural network [53]. Sensor changes can result in
707 changes in the signal-to-noise ratio and variance [54, 55], and the merging procedures
709 that produce a continuous data record generally do not account for data artefacts in
710 the higher statistical moments of the time series distribution [15, 56]. These may be
712 erroneously interpreted as signals of resilience loss [24].
714

715 **4.2 Resilience loss theory and detection**
716

717 EWS describe a set of statistical methods for detecting resilience loss, which are
718 based on the rationale that a systems' recovery rate to equilibrium after a disturbance
719 changes as the system loses resilience [15, 57].
720

721 A change in the recovery rate of a system can be measured by changes in auto-
722 correlation and variance [12]. Simultaneously increasing autocorrelation and variance
723 indicate both an increased tendency for the system properties to be distributed fur-
724 ther from its equilibrium, and a slower recovery back to its equilibrium: the basin of
725 attraction becomes wider and shallower. This indicates that a system's recovery rate
726 after disturbances or stochastic perturbations is slowing as the system state becomes
727 increasingly correlated with past states, termed **Critical Slowing Down (CSD)**.
728 CSD applies only when external conditions gradually move the system towards a
729
730
731
732
733
734
735
736

potential regime shift [58], also known as bifurcation tipping [59]. However, as natural systems are largely embedded in stochastic environments, the observability of a gradual increase in autocorrelation and variance alone may be limited [13, 24].	737 738 739 740 741 742 743 744 745 746 747 748 749 750 751 752 753 754 755 756 757 758 759 760 761 762 763 764 765 766 767 768 769 770 771 772 773 774 775 776 777 778 779 780 781 782
Recent studies have shown that the influence of multiple drivers, changes to the driving variable structure, or noise regime can modulate CSD signals, warranting attention not only to simultaneous increases, but also to mixed signals and simultaneous decreases [22, 23]. Research has shown experimentally that multiple drivers acting on a system simultaneously can produce contradictory signals [22]; increasing autocorrelation and decreasing variance, or vice-versa. Further, the dynamics of an ecosystem experiencing perturbations, such as increasing dry spells, may appear increasingly autocorrelated without approaching a critical threshold should the perturbation regime itself become increasingly autocorrelated [58]. They also find that the variance of the state variable may decrease prior to a critical threshold, should the state variables sensitivity to a forcing variable change over time.	760 761 762 763 764 765 766 767 768 769 770 771 772 773 774 775 776 777 778 779 780 781 782
Critical Speeding Up (CSU) is an alternative phenomenon of resilience loss and emerges in highly stochastic systems, given by a narrowing of the basin of attraction [23]. As this basin becomes smaller, the likelihood of a system occupying the smaller basin likewise becomes smaller, thereby reducing resilience, and leaving it more vulnerable to noise-induced (i.e. stochastic) transitions [23, 59]. With a single slowly changing forcing variables, decreasing autocorrelation and variance may indicate greater local stability. However, in stochastic environments, it may signal an increased vulnerability to noise associated with a shrinking basin of attraction.	760 761 762 763 764 765 766 767 768 769 770 771 772 773 774 775 776 777 778 779 780 781 782
Flickering is detected by changing skewness, and kurtosis or variance, and has been proposed as an alternative method for highly stochastic systems [60, 61]. Fundamentally, changes to the skewness and kurtosis of a system indicate an increasing	775 776 777 778 779 780 781 782

783 tendency for the system state to exist at the extremes of its distribution. Flicker-
784 ing measures brief excursions of the system to an alternative regime, where external
785 conditions may push the system temporarily closer to a critical threshold [13, 62, 63].
786

787 **The fractal dimension**, closely related to the Hurst Exponent, is a scale-free
788 measure of the self-similarity or long-term memory of a time series [64]. A decrease
789 in the fractal dimension indicates decreasing long-term memory, or increasing self-
790 similarity. While autocorrelation and variance may pick up an increase in noise over
791 time as a signal of resilience loss, the fractal dimension is more robust to this type of
792 non-stationarity in a time series [65].
793

794 In complex systems, multiple drivers affect the chosen state variable, each operating
795 on different temporal scales. Each driver may affect system recovery time and stability
796 in a way that is not captured by a single indicator. To account for this, we implement
797 a multiple working hypothesis approach [66]. We include assessments of five statistical
798 indicators typically included in EWS assessments: the autocorrelation and standard
799 deviation (CSD; [12, 13, 58, 67], CSU; [23]), skewness and kurtosis (flickering; [60,
800 62, 68]), and the fractal dimension [64, 65, 69]. For autocorrelation and standard
801 deviation, we also report regions showing mixed signals, where one increases and the
802 other decreases, and vice versa.
803

804 Because EWS are based on fluctuations of state variables about their equilibrium
805 [70], the time series are first de-trended and de-seasoned by applying a Seasonal-Trend
806 decomposition using LOESS filter to remove natural periodicities, inter-annual (1-
807 year) and inter-decadal modes of climate variability (5-years) [24]. Then, for all pixels,
808 the first difference of the resulting residual time series is used to calculate the EWS,
809 to remove as much residual periodicity from the time series as possible. To measure
810 the temporal evolution of autocorrelation, variance, skewness, kurtosis, and the fractal
811 dimension, we calculate each of the EWS indicators within a 5-year rolling window,
812 for each pixel globally (Figure 6).
813

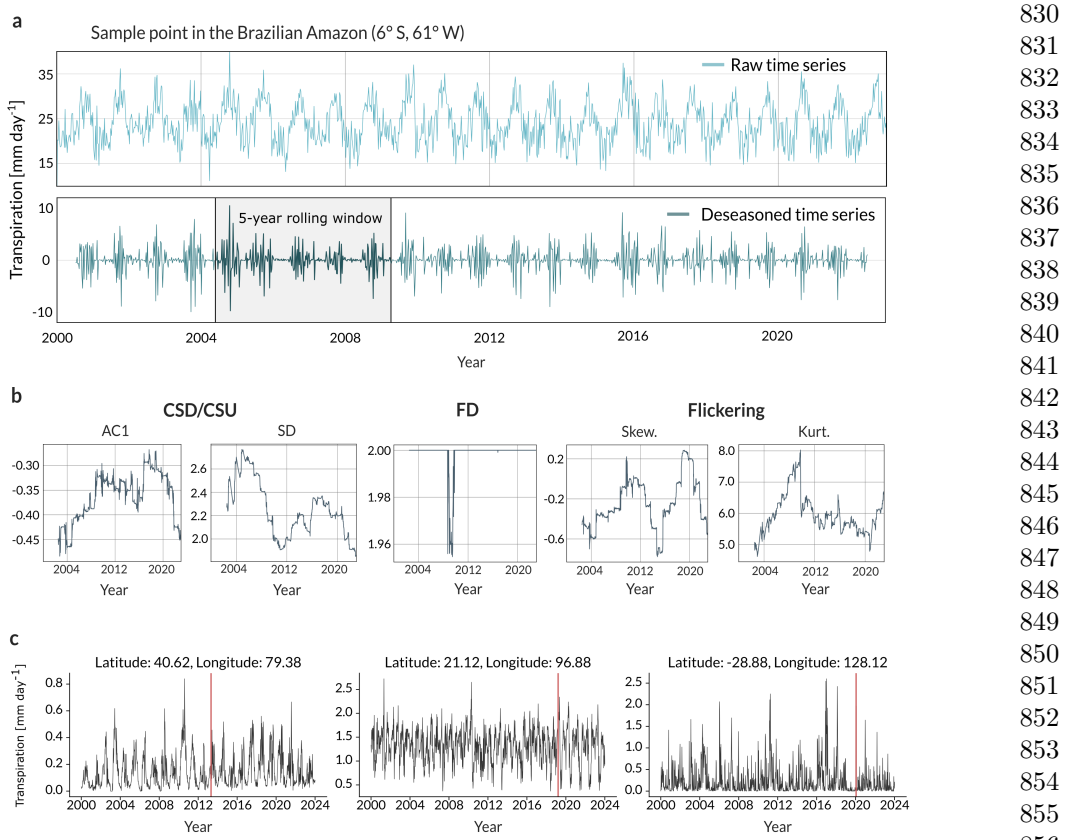


Fig. 6 Analysis example for transpiration. Panels (a - c) exemplify the analysis method used. (a) Raw and de-seasoned time series for transpiration for a pixel in the Brazilian Amazon, with 5-year rolling window over which the EWS are calculated, overlaid. (b) Five indicators are computed for the pixel on the de-seasoned time series, over the rolling window. Autocorrelation (AC1) and standard deviation (SD) are associated with Critical Slowing Down (CSD) and Critical Speeding Up (CSU); skewness (Skew.), and kurtosis (Kurt.) are associated with flickering; the fractal dimension (FD) is interpreted alone. (c) Exemplary pixels where an abrupt shift in transpiration was detected; the red vertical line marks the estimated year of shift.

We calculate three different statistics of the change in the five EWS indicators to obtain a comprehensive understanding: the Kendall's τ is used to determine the significance of a monotonic trend [71]; the Thiel-Sen slope is used to quantify the magnitude of the trend [72, 73]; and the change in mean at half the time series is used to quantify the overall shift between the first and second half of the time-series, where significance was determined using a two-sided t -test [19]. For a comparison of the

875 agreement across tests, see Supplementary Fig. 6. As an additional measure, we calcu-
876 late the time-ordered difference between maximum and minimum of each EWS, delta,
877 to yield the maximum change over the time-series length [16]. For the computation of
878 statistics, we exclude pixels that contain more than 3% built environment using land
880 cover masks from the Copernicus Global Land Service [74]. Pixels that contain more
882 than 25% crop cover and are predominantly non-irrigated (based on area equipped for
884 irrigation [75]) are treated separately as an artificial rain-fed cropland biome.
886
887

888 **4.3 Estimating abrupt shifts**

889

890 We identify abrupt shifts for the three green water variables using the raw variable
891 time series. The set of identified abrupt shifts serves as empirical ground-truth of
892 where green water dynamics have abruptly and significantly changed. Abrupt shifts
893 are detected using the R package 'strucchange' [76, 77], which is a breakpoint detection
894 method which applies a structural change test to fitted autoregressive model (AR1)
895 of the time series. For each pixel, we fit an autoregressive model, where the variable
896 at time x_t is regressed on its lag at x_{t-1} , and computed the supF statistic [26]. A
897 breakpoint is identified at the time where the regression intercept (mean) and/or
898 the autoregressive processes governing the time series changed significantly ($p < 0.05$
899 from the supF test). We interpreted these breakpoints as the point in time when
900 short-term dynamics governing the time series change, thus representing abrupt shifts
901 in variable dynamics. We then compute the mean before (m_1) and after (m_2) the
902 breakpoint, and report both absolute ($m_2 - m_1$) and proportional (m_2/m_1) changes.
903 We report the results from the structural change approach, because it is statistically
904 more conservative and appears less prone to spurious detections than tests based solely
905 on mean or variance shift, given that it jointly tests for shifts in mean and short-term
906 memory processes.
907
908
909
910
911
912
913
914
915
916
917
918
919
920

4.4 Evaluating EWS efficacy

We assume that, should a structural change in green water properties at a pixel have occurred, such a change would manifest as a detected abrupt shift in the time series, with a preceding EWS. To better understand if EWS can predict the detected abrupt shift binary target, we developed a machine learning framework to train three boosted regression classification models, one for each green water variable. Boosted regression models are tree-based machine learning models that are able to capture interactions and non-linear patterns between predictor variables [78]. The target variables for each model were whether or not an abrupt shift was detected (True/False; positive or negative class, respectively), and the features, or explanatory variables used to predict the target variable, are the Kendall's τ of the EWS (Section 4.2) and several environmental variables to represent the hydrological, ecological, and climatic features of each pixel. The environmental variables included in the models, the green water variable for which they were applied, and dataset sources listed in Supplementary Table 9. The environmental variables were resampled to a 0.25° spatial resolution to match the resolution of the target variables, and resampled to monthly time-scales where needed. These variables were added as static features: including only the mean, standard deviation, and linear trend over time of the variable.

To prevent systematic distributional differences of the EWS Kendall's τ between the positive and negative classes being picked up by the models, the EWS feature variables were created separately and then combined with the environmental variables. For the positive class, we re-calculated the EWS and Kendall's τ on the time series preceding the abrupt shift. We did this for all pixels where the breakpoints detected using the supF-statistic were significant, and occurred at least 12 years after the start of the time series, to ensure a sufficient number of time steps for the EWS calculation and to account for the rolling window length. For the negative class, to construct the EWS variables in a symmetrical way, we generate a distribution of breakpoint time

967 stamps from the positive class, and randomly sample time steps from this distribu-
968 tion, assigning them to pixels in the negative class. We then re-calculate Kendall's
969 τ of the EWS before this randomly assigned breakpoint, or pseudo-breakpoint. The
970 explanatory variables in the models therefore include the Kendall's τ of each of the
971 five studied EWS (Section 4.2) either before the breakpoint for the positive class, or
972 before a pseudo-breakpoint for the negative class, and the environmental variables
973 over the whole time series. Machine learning models are not based on a mechanis-
974 tic representation of processes, so they cannot directly provide causal information on
975 how features influence the system response. Rather, the explanatory variables describe
976 environmental characteristics and EWS signals, at each pixel that may contribute to
977 the detection of an abrupt shift.

978 Because positive cases (detected abrupt shifts) are relatively rare at the global
979 scale, we apply a class weighting to address class imbalance. We retain the full
980 dataset, but apply a weight proportional to the negative-to-positive class ratio during
981 model training and performance evaluation. Given that breakpoints were clustered in
982 space, we implement a spatial, blocked cross-validation to account for potential spa-
983 tial autocorrelation [79]. Specifically, the global domain was partitioned into $10^\circ \times 10^\circ$
984 latitude-longitude blocks where each block is randomly assigned to one of five cross-
985 validation folds, or subsets, so calibration and validation occurs on spatially separated
986 regions. This results in an 80% and 20% training and testing split. The 10° size was
987 chosen as a practical compromise between reducing spatial leakage and retaining suffi-
988 ciently heterogenous training data per subset. Model performance is therefore assessed
989 by training the model on four subsets, and evaluating on the held-out fifth, for all five
990 subsets [79]. Further details on the model training can be found in Supplementary
991 Table 10 and Supplementary Fig. 11. Given that the abrupt shifts detected are rela-
992 tively rare events, we report the precision-recall area-under-the-curve (PR AUC) and
993
994
995
996
997
998
999
1000
1001
1002
1003
1004
1005
1006
1007
1008
1009
1010
1011
1012

average precision (AP) to quantify model performance as threshold-agnostic performance metrics that remains informative under significant imbalance between positive and negative classes [80]. We then calculate Partial Dependence Plots (PDPs; [78]) and SHAP values [81] to provide explanations of feature effects and contributions to detecting abrupt shifts. To isolate the predictive value of EWS as predictors relative to the environmental variables as predictors, we also train two additional models per green water variable that contain either only the EWS as predictors, only the environmental variables as predictors, and compare these to the model performance with the full predictor set.

4.5 Sensitivity analysis

We conduct a sensitivity analysis to verify that our inferences are robust across calculation set-ups. We calculate the EWS and Kendall's τ for a 50 by 50 pixel tile, or 12.5° by 12.5° , in South America. We vary: (1) the sampling frequency (weekly, monthly), (2) window size over which EWS are calculated (2.5-years, 5-years, 10-years), and (3) de-trending choices (STL robust; first-differencing). For each configuration we map the Kendall's τ sign to three class labels ($-1, 0, +1$; negative τ , no change, positive τ), where $|\tau| \leq 0.05$ and $p > 0.05$ are treated as 0. For each configuration, we calculate the pair-wise Cohen's κ [82] and report the average agreement across all configurations, adjusted for chance (Light's κ [83]). This allows us to capture whether two configurations give the same sign, or show no change, at the same pixel, measuring the pixel-wise agreement between chosen parameter configurations. Cohen's κ denotes how much two maps of Kendall's τ agree on the sign of change, beyond what would be expected by chance, where $\kappa = 1$ is perfect agreement, $\kappa = 0$ is no better than chance, and $\kappa < 0$ indicates disagreement. To measure the effect of one configuration change, we create pairs of configurations that are identical on the other three factors and differ only in the configuration we want to measure the effect of. We then compute Cohen's

1059 κ for each such pairs maps, averaging κ across the pairs. Light's κ is the pairwise
1060 average κ across all configurations, calculated per indicator (Supplementary Table 1).
1061

1062 **Transpiration.** Across configurations, Light's κ is highest for AC1 ($\kappa = 0.16$), fol-
1063 lowed by FD, kurtosis, SD, and skewness (mean κ across indicators = 0.116). Sampling
1064 frequency (weekly vs. monthly) is the largest source of sensitivity (mean κ across indi-
1065 cators = -0.01), indicating systematic pixel-wise disagreement between monthly and
1066 1069 weekly data. Changing only the window length gives a mean κ of 0.4 across indicators,
1070 1071 indicating relative stability. First differencing has a lower mean κ across indicators
1072 1073 (0.24), indicating moderate stability (Supplementary Table 1).
1073

1074 **Soil moisture.** Overall agreement is higher for soil moisture across configurations;
1075
1076 SD is most stable (Light's $\kappa = 0.56$), followed by kurtosis, FD, AC1, and skewness
1077 (mean κ across indicators = 0.23). First differencing is the largest source of sensitivity,
1078 1079 resulting in the lowest mean κ for AC1, FD, kurtosis, and skewness (0.16, 0.06, 0.11,
1080 1081 -0.03, respectively); SD remains high (0.71). Changing either only the window length
1082 1083 or sampling frequency results in a higher agreement (mean κ across indicators = 0.487
1083
1084 and 0.318, respectively) (Supplementary Table 1).
1085

1086 **Precipitation.** Light's κ is highest for SD ($\kappa = 0.30$), followed by AC1, FD,
1087 1088 kurtosis and skewness (κ across indicators = 0.19). Sampling frequency is again the
1089 1090 largest source of sensitivity, having the greatest effect on pixel-wise sign agreement.
1091 1092 Between weekly and monthly temporal aggregation, mean κ is 0.17 for SD and ≈ 0.03
1093 1094 for the remaining variables. With a fixed sampling frequency, mean κ is higher for the
1095 1096 other configurations. Changing window lengths gives mean $\kappa = 0.52$ across EWS. The
1097 1098 first differencing configuration gives mean $\kappa = 0.36$, for SD, AC1, FD, and kurtosis.
1099 1100 Skewness is sensitive to first differencing (mean $\kappa = -0.03$), signalling disagreement
1101 1102 (Supplementary Table 1).
1103

1104 1105 We choose weekly sampling frequency to preserve seasonal variability and maximise
1106 1107 observations per sampling window, although we note that results are sensitive to the
1108
1109

chosen sampling frequency. Given that results are relatively stable across window lengths, we choose a 5-year window as a compromise between adequate sample size and temporal smoothening. 1105
1106
1107
1108
1109
1110
1111
1112
1113
1114
1115
1116
1117
1118
1119
1120
1121
1122
1123
1124
1125
1126
1127
1128
1129
1130
1131
1132
1133
1134
1135
1136
1137
1138
1139
1140
1141
1142
1143
1144
1145
1146
1147
1148
1149
1150

Further, to assess the sensitivity of the results to trend estimation approach, we compare three approaches for each indicator (AC1, SD, FD, Skew, Kurt) and check for agreement in sign of change: KT (Kendall's τ , $p < 0.05$), TS (Theil–Sen slope, $p < 0.05$), Δ (time-ordered difference between maximum and minimum), and MC (mean-change between time series halves, Welch's t-test $p < 0.05$) (Supplementary Fig. 6). Each pixel is assigned a class of -1, 0, or +1 (corresponding to a decrease, no change, or an increase). The pairwise comparisons use all grid cells ($n = 1\,036\,800$). We report the linear-weighted Cohen's κ [82]. Weights are 1 where both show agreement in sign, 0.5 where signs are adjacent (i.e. increasing and no change, or decreasing and no change), and 0 for opposite signs. KT and TS slope agree for AC1, SD, Skew., Kurt. ($\kappa_w \geq 0.997$) on trend direction across variables (Supplementary Fig. 6). MC vs KT/TS shows high agreement for AC1, SD, Skew., Kurt. ($\kappa_w \approx 0.85\text{--}0.89$). The time-ordered difference (δ) has very low agreement with other tests ($\kappa_w \approx 0.02\text{--}0.07$). Relatively fewer pixels that showed a significant change in FD were detected using the Theil-Sen test, which therefore shows weak agreement with MC and KT across green water variables ($0.05 \leq \kappa_w \leq 0.25$). While AC1, SD, Skew., and Kurt. show strong agreement across methods, we find FD is sensitive to the choice of trend estimator.

Supplementary information. This article has accompanying supplementary information.

Acknowledgements. We thank M. Kummu and A. Hattle for their helpful comments on the manuscript.

1151 **Declarations**

1152

1153

1154 **5 Funding**

1155

1156 This manuscript is a product of the Formas project SAFER with grant number
1157
1158 2022-02089. Additionally, L.W-E is further supported by funding from Formas - a
1159
1160 Swedish Research Council for Sustainable Development (ESI 2023-00310, ReForMit
1161 2023-00321, and SOS-Cryo 2024-01655), the IKEA foundation, and Horizon Europe
1162
1163 (WorldTrans 101081661); J.C.R. and N.K. are supported by VR grant 2022-04122.

1164

1165

1166 **6 Competing interests**

1167

1168

1169 The authors declare no competing interests.

1170

1171

1172 **7 Ethics approval and consent to participate**

1173

1174 Not applicable

1175

1176

1177 **8 Consent for publication**

1178

1179 Not applicable

1180

1181

1182

1183 **9 Data availability**

1184

1185 All data was retrieved from publicly available, open datasets: GLEAM version 4.2
1186

1187 daily transpiration (<https://www.gleam.eu/>); PERSIANN-CDR daily precipitation
1188

1189 (<https://chrsdata.eng.uci.edu/>); ESA-CCI SM combined sensor daily soil moisture
1190

1191 (<https://climate.esa.int/en/projects/soil-moisture/>); Copernicus Land Monitoring

1192 Service crop and urban land cover fractions (<https://land.copernicus.eu/en/global>).

1193

1194 For the machine learning analysis 2-meter temperature, 2-meter dew-point

1195

1196

temperature, relative humidity, total precipitation, volumetric soil moisture, transpiration, boundary layer height, convective available potential energy, and forecast albedo, were retrieved from the Earth Retrospective Analysis 5 (ERA5) monthly averaged data on single levels (<https://cds.climate.copernicus.eu/datasets/reanalysis-era5-single-levels-monthly-means>); hourly potential evapotranspiration was retrieved from (ref.[84], <https://doi.org/10.5523/bris.qb8ujazzda0s2aykkv0oq0ctp>); groundwater table depth was retrieved from (ref.[85], <http://thredds-gfnl.usc.es/thredds/catalog/GLOBALWTDFTP/catalog.html>); crop cover data was retrieved from Global Food-and-Water Security-support Analysis Data (GFSAD) (<https://www.usgs.gov/centers/western-geographic-science-center/science/global-food-and-water-security-support-analysis>); MODIS/Terra Gross Primary Productivity 8-Day L4 Global 500m SIN Grid V061 was retrieved from (<https://www.earthdata.nasa.gov/data/catalog/lpcloud-mod17a2h-061>); tree cover and non-tree vegetation cover were retrieved from MODIS-/Terra Vegetation Continuous Fields Yearly L3 Global 250m SIN Grid V006 (<https://www.earthdata.nasa.gov/data/catalog/lpcloud-mod44b-006>); ENSO index was retrieved from NASA-SSH ENSO Sea Surface Height Indicator (https://podaac.jpl.nasa.gov/dataset/NASA_SSH_ENSO_INDICATOR).

10 Materials availability

Not applicable

11 Code availability

All code used in the analysis of the raw data to produce the primary results is available on GitHub (https://github.com/romlotch/25_09_water_resilience_ews).

1243 **12 Author contribution**

1244

1245 **R.L.**: Conceptualization, Methodology, Software, Validation, Formal analysis, Inves-
1246

1247 tigation, Writing – original draft, Writing – review & editing, Visualization. **N.K.**:
1248

1249 Software, Writing – review & editing. **L.W-E.**: Conceptualisation, Investigation, Writ-
1250 ing – review & editing, Supervision, Project administration, Funding acquisition.
1251

1252 **J.C.R.**: Conceptualisation, Investigation, Writing – review & editing, Supervision,
1253 Project administration, Funding acquisition.
1254

1255

1256

1257

1258

1259

1260

1261

1262

1263

1264

1265

1266

1267

1268

1269

1270

1271

1272

1273

1274

1275

1276

1277

1278

1279

1280

1281

1282

1283

1284

1285

1286

1287

1288

Appendix A Extended Data

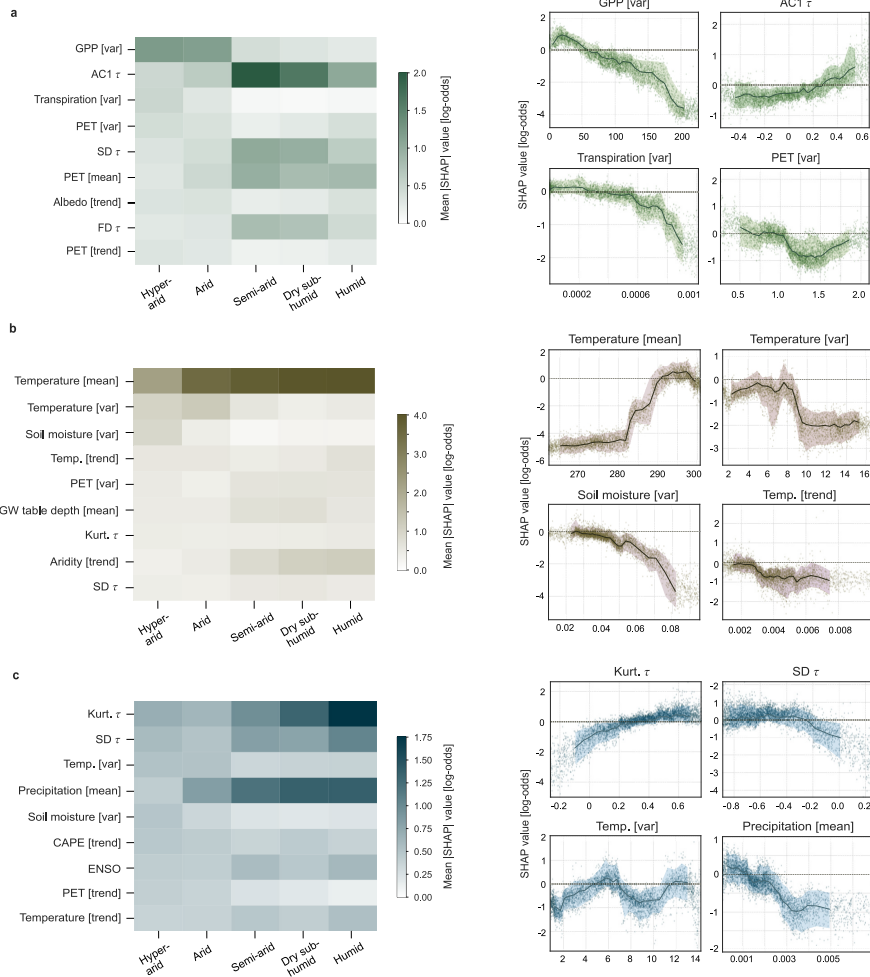
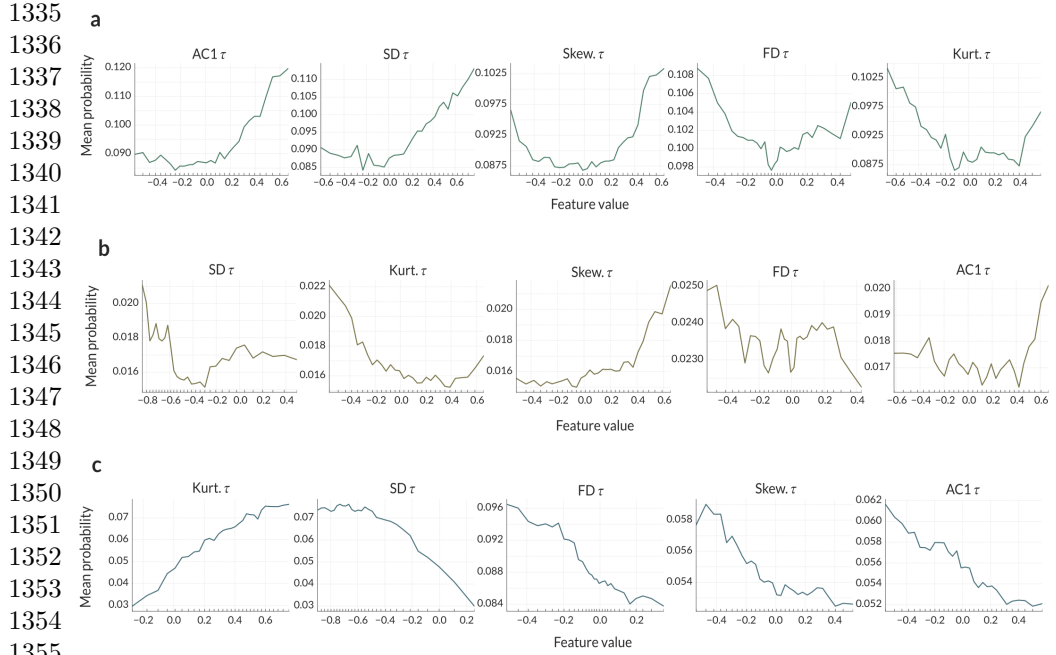


Fig. A1 Model interpretability with SHAP values across aridity classes for transpiration (a), soil moisture (b), and precipitation (c). Heatmaps show SHAP values for the top 10 predictors with the highest contribution to the model predictions, with rows organised by mean absolute SHAP importance across aridity classes, and SHAP dependence plots of the four most important predictors, show feature value (x-axis) against SHAP log-odds (y-axis), representing its contribution to model predictions. Positive values increase the predicted probability of an abrupt shift, negative values decrease it.

1289
1290
1291
1292
1293
1294
1295
1296
1297
1298
1299
1300
1301
1302
1303
1304
1305
1306
1307
1308
1309
1310
1311
1312
1313
1314
1315
1316
1317
1318
1319
1320
1321
1322
1323
1324
1325
1326
1327
1328
1329
1330
1331
1332
1333
1334



1362 References

1363

1364

1365 [1] Gleeson, T. *et al.* Illuminating water cycle modifications and Earth system
1366 resilience in the Anthropocene. *Water Resources Research* **56** (2020). Publisher:
1367 American Geophysical Union (AGU).

1368

1369

1370 [2] Falkenmark, M. & Wang-Erlandsson, L. A water-function-based framework for
1371 understanding and governing water resilience in the Anthropocene. *One Earth*
1372 **4**, 213–225 (2021). Publisher: Elsevier BV.

1373

1374

1375

1376 [3] Wang-Erlandsson, L. *et al.* A planetary boundary for green water. *Nature Reviews
1377 Earth & Environment* **3**, 380–392 (2022). Publisher: Springer

1378

1379

1380

Science and Business Media LLC. 1381
1382

[4] Porkka, M. *et al.* Global water cycle shifts far beyond pre-industrial conditions – planetary boundary for freshwater change transgressed (2023). Publisher: California Digital Library (CDL). 1383
1384
1385
1386
1387
1388
1389
1390
1391
1392
1393
1394
1395
1396
1397
1398
1399

[5] Nie, W. *et al.* Nonstationarity in the global terrestrial water cycle and its interlinkages in the Anthropocene. *Proceedings of the National Academy of Sciences* **121**, e2403707121 (2024). URL <https://www.pnas.org/doi/abs/10.1073/pnas.2403707121>. Company: National Academy of Sciences Distributor: National Academy of Sciences Institution: National Academy of Sciences Label: National Academy of Sciences Publisher: Proceedings of the National Academy of Sciences. 1400
1401
1402
1403
1404
1405
1406
1407
1408
1409
1410
1411
1412
1413
1414

[6] Falkenmark, M., Wang-Erlandsson, L. & Rockström, J. Understanding of water resilience in the Anthropocene. *Journal of Hydrology X* **2**, 100009 (2019). Publisher: Elsevier BV. 1415
1416
1417
1418

[7] Zemp, D. C., Schleussner, C.-F., Barbosa, H. M. J. & Rammig, A. Deforestation effects on Amazon forest resilience. *Geophysical Research Letters* **44**, 6182–6190 (2017). URL <https://onlinelibrary.wiley.com/doi/abs/10.1002/2017GL072955>.
_eprint: <https://onlinelibrary.wiley.com/doi/pdf/10.1002/2017GL072955>. 1419
1420
1421
1422
1423
1424
1425
1426

[8] Staal, A. *et al.* Feedback between drought and deforestation in the Amazon. *Environmental Research Letters* **15**, 044024 (2020). URL <https://dx.doi.org/10.1088/1748-9326/ab738e>. Publisher: IOP Publishing. 1427
1428

[9] Yang, L., Sun, G., Zhi, L. & Zhao, J. Negative soil moisture-precipitation feedback in dry and wet regions. *Scientific Reports* **8** (2018). Publisher: Springer Science and Business Media LLC. 1429
1430
1431
1432
1433
1434
1435
1436
1437
1438

1427 [10] Berdugo, M. *et al.* Global ecosystem thresholds driven by aridity. *Science* **367**,
1428 787–790 (2020). Publisher: American Association for the Advancement of Science
1429 (AAAS).

1430

1431

1432 [11] Holling, C. S. Resilience and Stability of Ecological Systems. *Annual Review of*
1433 *Ecology and Systematics* **4**, 1–23 (1973). Publisher: Annual Reviews.

1434

1435

1436 [12] Scheffer, M. *et al.* Early-warning signals for critical transitions. *Nature* **461**,
1437 53–59 (2009). Publisher: Springer Science and Business Media LLC.

1438

1439

1440 [13] Dakos, V., Carpenter, S. R., van Nes, E. H. & Scheffer, M. Resilience indicators:
1441 prospects and limitations for early warnings of regime shifts. *Philosophical Trans-*
1442 *actions of the Royal Society B: Biological Sciences* **370**, 20130263 (2015). URL
1443 <https://royalsocietypublishing.org/doi/full/10.1098/rstb.2013.0263>. Publisher:
1444 Royal Society.

1445

1446 [14] Dakos, V. & Kéfi, S. Ecological resilience: what to measure and how. *Environ-*
1447 *mental Research Letters* **17**, 043003 (2022). Publisher: IOP Publishing.

1448

1449 [15] Dakos, V. *et al.* Tipping point detection and early warnings in climate, ecological,
1450 and human systems. *Earth System Dynamics* **15**, 1117–1135 (2024). Publisher:
1451 Copernicus GmbH.

1452

1453 [16] Rocha, J. C. Ecosystems are showing symptoms of resilience loss. *Environmental*
1454 *Research Letters* **17**, 065013 (2022). Publisher: IOP Publishing.

1455

1456 [17] Smith, T., Traxl, D. & Boers, N. Empirical evidence for recent global shifts in
1457 vegetation resilience. *Nature Climate Change* **12**, 477–484 (2022). URL <https://www.nature.com/articles/s41558-022-01352-2>. Publisher: Nature Publishing
1458 Group.

1459

1460

1461

1462

1463

1464

1465

1466

1467

1468

1469

1470

1471

1472

[18] Feng, Y. *et al.* Reduced resilience of terrestrial ecosystems locally is not reflected on a global scale. *Communications Earth & Environment* **2**, 1–11 (2021). URL <https://www.nature.com/articles/s43247-021-00163-1>. Publisher: Nature Publishing Group. 1473
1474
1475
1476
1477
1478
1479
1480
1481
1482
1483
1484
1485
1486
1487
1488
1489
1490
1491
1492
1493
1494
1495
1496
1497
1498
1499
1500
1501
1502
1503
1504
1505
1506
1507
1508
1509
1510
1511
1512
1513
1514
1515
1516
1517
1518

[19] Forzieri, G., Dakos, V., McDowell, N. G., Ramdane, A. & Cescatti, A. Emerging signals of declining forest resilience under climate change. *Nature* **608**, 534–539 (2022). URL <https://www.nature.com/articles/s41586-022-04959-9>. Publisher: Nature Publishing Group. 1480
1481
1482
1483
1484
1485
1486
1487
1488
1489
1490
1491
1492
1493
1494
1495
1496
1497
1498
1499
1500
1501
1502
1503
1504
1505
1506
1507
1508
1509
1510
1511
1512
1513
1514
1515
1516
1517
1518

[20] Verbesselt, J. *et al.* Remotely sensed resilience of tropical forests. *Nature Climate Change* **6**, 1028–1031 (2016). URL <https://www.nature.com/articles/nclimate3108>. Publisher: Nature Publishing Group. 1480
1481
1482
1483
1484
1485
1486
1487
1488
1489
1490
1491
1492
1493
1494
1495
1496
1497
1498
1499
1500
1501
1502
1503
1504
1505
1506
1507
1508
1509
1510
1511
1512
1513
1514
1515
1516
1517
1518

[21] Knecht, N., Lotcheris, R. A., Fetzer, I. & Rocha, J. Complex Realities, Simple Signals? Global Evaluation of Early Warning Signals for Forest Mortality Events. *EGUphere* 1–42 (2025). URL <https://eguphre.copernicus.org/preprints/2025/eguphre-2025-4902/>. Publisher: Copernicus GmbH. 1480
1481
1482
1483
1484
1485
1486
1487
1488
1489
1490
1491
1492
1493
1494
1495
1496
1497
1498
1499
1500
1501
1502
1503
1504
1505
1506
1507
1508
1509
1510
1511
1512
1513
1514
1515
1516
1517
1518

[22] Dai, L., Korolev, K. S. & Gore, J. Relation between stability and resilience determines the performance of early warning signals under different environmental drivers. *Proceedings of the National Academy of Sciences* **112**, 10056–10061 (2015). Publisher: Proceedings of the National Academy of Sciences. 1480
1481
1482
1483
1484
1485
1486
1487
1488
1489
1490
1491
1492
1493
1494
1495
1496
1497
1498
1499
1500
1501
1502
1503
1504
1505
1506
1507
1508
1509
1510
1511
1512
1513
1514
1515
1516
1517
1518

[23] Titus, M. & Watson, J. Critical speeding up as an early warning signal of stochastic regime shifts. *Theoretical Ecology* **13**, 449–457 (2020). URL <https://doi.org/10.1007/s12080-020-00451-0>. 1480
1481
1482
1483
1484
1485
1486
1487
1488
1489
1490
1491
1492
1493
1494
1495
1496
1497
1498
1499
1500
1501
1502
1503
1504
1505
1506
1507
1508
1509
1510
1511
1512
1513
1514
1515
1516
1517
1518

[24] Smith, T. & Boers, N. Reliability of vegetation resilience estimates depends on biomass density. *Nature Ecology & Evolution* **7**, 1799–1808 (2023). 1480
1481
1482
1483
1484
1485
1486
1487
1488
1489
1490
1491
1492
1493
1494
1495
1496
1497
1498
1499
1500
1501
1502
1503
1504
1505
1506
1507
1508
1509
1510
1511
1512
1513
1514
1515
1516
1517
1518

1519 Publisher: Springer Science and Business Media LLC.
1520

1521 [25] Boettiger, C. & Hastings, A. No early warning signals for stochastic transitions:
1522 1523 insights from large deviation theory. *Proceedings of the Royal Society B: Biological
1524 Sciences* **280**, 20131372 (2013). Publisher: The Royal Society.
1525

1526

1527 [26] Andersen, T., Carstensen, J., Hernández-García, E. & Duarte, C. M. Ecologi-
1528 1529 cal thresholds and regime shifts: approaches to identification. *Trends in Ecology
1530 & Evolution* **24**, 49–57 (2009). URL <https://www.sciencedirect.com/science/article/pii/S0169534708003054>.
1531

1532

1533 [27] Smith, T. & Boers, N. Global vegetation resilience linked to water availability and
1534 1535 variability. *Nature Communications* **14**, 498 (2023). URL <https://www.nature.com/articles/s41467-023-36207-7>. Publisher: Nature Publishing Group.
1536

1537

1538 [28] Seddon, A. W. R., Macias-Fauria, M., Long, P. R., Benz, D. & Willis, K. J.
1539 1540 Sensitivity of global terrestrial ecosystems to climate variability. *Nature* **531**,
1541 1542 229–232 (2016). URL <https://www.nature.com/articles/nature16986>. Publisher:
1543 1544 Nature Publishing Group.
1545

1546

1547

1548 [29] Huang, J., Yu, H., Guan, X., Wang, G. & Guo, R. Accelerated dryland expansion
1549 1550 under climate change. *Nature Climate Change* **6**, 166–171 (2016). URL <https://www.nature.com/articles/nclimate2837>. Publisher: Nature Publishing Group.
1551

1552

1553 [30] Li, W. *et al.* Widespread increasing vegetation sensitivity to soil moisture. *Nature
1554 Communications* **13**, 3959 (2022). URL <https://www.nature.com/articles/s41467-022-31667-9>. Publisher: Nature Publishing Group.
1555

1556

1557

1558 [31] Boulton, C. A., Lenton, T. M. & Boers, N. Pronounced loss of Amazon rainforest
1559 1560 resilience since the early 2000s. *Nature Climate Change* **12**, 271–278 (2022).
1561

1562 URL <https://www.nature.com/articles/s41558-022-01287-8>. Publisher: Nature
1563

1564

Publishing Group.	1565
	1566
[32] Walvoord, M. A. & Kurylyk, B. L. Hydrologic Impacts of Thawing Permafrost—A Review. <i>Vadose Zone Journal</i> 15 , vzb2016.01.0010 (2016). URL https://doi.org/10.2136/vzj2016.01.0010 .	1567
	1568
	1569
	1570
	1571
	1572
[33] Calvin, K. <i>et al.</i> IPCC, 2023: Climate Change 2023: Synthesis Report. Contribution of Working Groups I, II and III to the Sixth Assessment Report of the Intergovernmental Panel on Climate Change [Core Writing Team, H. Lee and J. Romero (eds.)]. IPCC, Geneva, Switzerland. Tech. Rep., Intergovernmental Panel on Climate Change (IPCC) (2023). URL https://www.ipcc.ch/report/ar6/syr/ . Edition: First.	1573
	1574
	1575
	1576
	1577
	1578
	1579
	1580
	1581
	1582
	1583
[34] Myers-Smith, I. H. <i>et al.</i> Shrub expansion in tundra ecosystems: dynamics, impacts and research priorities. <i>Environmental Research Letters</i> 6 , 045509 (2011). URL https://dx.doi.org/10.1088/1748-9326/6/4/045509 . Publisher: IOP Publishing.	1584
	1585
	1586
	1587
	1588
	1589
	1590
	1591
	1592
	1593
	1594
	1595
	1596
	1597
	1598
[35] Macias-Fauria, M., Forbes, B. C., Zetterberg, P. & Kumpula, T. Eurasian Arctic greening reveals teleconnections and the potential for structurally novel ecosystems. <i>Nature Climate Change</i> 2 , 613–618 (2012). URL https://www.nature.com/articles/nclimate1558 . Publisher: Nature Publishing Group.	1599
	1600
	1601
	1602
	1603
	1604
	1605
	1606
	1607
	1608
	1609
	1610
[36] Zhang, Y. <i>et al.</i> Warming and disturbances affect Arctic-boreal vegetation resilience across northwestern North America. <i>Nature Ecology & Evolution</i> 8 , 2265–2276 (2024). URL https://www.nature.com/articles/s41559-024-02551-0 . Publisher: Nature Publishing Group.	35
[37] Porkka, M. <i>et al.</i> Notable shifts beyond pre-industrial streamflow and soil moisture conditions transgress the planetary boundary for freshwater change.	

1611 *Nature Water* **2**, 262–273 (2024). URL <https://www.nature.com/articles/s44221-024-00208-7>. Publisher: Nature Publishing Group.

1612

1613

1614

1615 [38] Kéfi, S., Rietkerk, M., van Baalen, M. & Loreau, M. Local facilitation,
1616 bistability and transitions in arid ecosystems. *Theoretical Population Biology*
1617 **71**, 367–379 (2007). URL <https://www.sciencedirect.com/science/article/pii/S0040580906001250>.

1618

1619

1620

1621

1622

1623 [39] Gentine, P. *et al.* Coupling between the terrestrial carbon and water cycles—a
1624 review. *Environmental Research Letters* **14**, 083003 (2019). URL <https://dx.doi.org/10.1088/1748-9326/ab22d6>. Publisher: IOP Publishing.

1625

1626

1627

1628 [40] Bassiouni, M., Good, S. P., Still, C. J. & Higgins, C. W. Plant
1629 Water Uptake Thresholds Inferred From Satellite Soil Moisture. *Geo-
1630*
1631 *physical Research Letters* **47**, e2020GL087077 (2020). URL <https://onlinelibrary.wiley.com/doi/abs/10.1029/2020GL087077>. eprint:
1632

1633 <https://agupubs.onlinelibrary.wiley.com/doi/pdf/10.1029/2020GL087077>.

1634

1635

1636

1637 [41] Seneviratne, S. I. *et al.* Investigating soil moisture–climate interactions in a
1638 changing climate: A review. *Earth-Science Reviews* **99**, 125–161 (2010). URL
1639 <https://www.sciencedirect.com/science/article/pii/S0012825210000139>.

1640

1641

1642

1643 [42] Zhang, Q. *et al.* Water limitation regulates positive feedback of increased ecosys-
1644 tem respiration. *Nature Ecology & Evolution* **8**, 1870–1876 (2024). URL <https://www.nature.com/articles/s41559-024-02501-w>. Publisher: Nature Publishing
1645

1646

1647

1648

1649

1650

1651 [43] Rocha, J. C., Peterson, G., Bodin, & Levin, S. Cascading regime shifts within and
1652 across scales. *Science* **362**, 1379–1383 (2018). URL <https://www.science.org/doi/10.1126/science.aat7850>. Publisher: American Association for the Advancement
1653

1654

1655

1656 of Science.

[44] Zhou, G. *et al.* Resistance of ecosystem services to global change weakened by increasing number of environmental stressors. *Nature Geoscience* **17**, 882–888 (2024). URL <https://www.nature.com/articles/s41561-024-01518-x>. Publisher: Nature Publishing Group. 1657
1658
1659
1660
1661
1662
1663
1664
1665
1666
1667
1668
1669
1670
1671
1672
1673
1674
1675
1676
1677
1678
1679
1680
1681
1682
1683
1684
1685
1686
1687
1688
1689
1690
1691
1692
1693
1694
1695
1696
1697
1698
1699
1700
1701
1702

[45] Kornhuber, K. *et al.* Amplified Rossby waves enhance risk of concurrent heat-waves in major breadbasket regions. *Nature Climate Change* **10**, 48–53 (2019). Publisher: Springer Science and Business Media LLC. 1664
1665
1666
1667
1668
1669
1670
1671
1672
1673
1674
1675
1676
1677
1678
1679
1680
1681
1682
1683
1684
1685
1686
1687
1688
1689
1690
1691
1692
1693
1694
1695
1696
1697
1698
1699
1700
1701
1702

[46] Hu, K., Huang, G., Huang, P., Kosaka, Y. & Xie, S.-P. Intensification of El Niño-induced atmospheric anomalies under greenhouse warming. *Nature Geoscience* **14**, 377–382 (2021). URL <https://www.nature.com/articles/s41561-021-00730-3>. Publisher: Nature Publishing Group. 1670
1671
1672
1673
1674
1675
1676
1677
1678
1679
1680
1681
1682
1683
1684
1685
1686
1687
1688
1689
1690
1691
1692
1693
1694
1695
1696
1697
1698
1699
1700
1701
1702

[47] Miralles, D. G. *et al.* GLEAM4: global land evaporation and soil moisture dataset at 0.1° resolution from 1980 to near present. *Scientific Data* **12**, 416 (2025). URL <https://www.nature.com/articles/s41597-025-04610-y>. Publisher: Nature Publishing Group. 1670
1671
1672
1673
1674
1675
1676
1677
1678
1679
1680
1681
1682
1683
1684
1685
1686
1687
1688
1689
1690
1691
1692
1693
1694
1695
1696
1697
1698
1699
1700
1701
1702

[48] Dorigo, W. *et al.* ESA CCI Soil Moisture for improved Earth system understanding: State-of-the art and future directions. *Remote Sensing of Environment* **203**, 185–215 (2017). URL <https://www.sciencedirect.com/science/article/pii/S0034425717303061>. 1685
1686
1687
1688
1689
1690
1691
1692
1693
1694
1695
1696
1697
1698
1699
1700
1701
1702

[49] Gruber, A., Scanlon, T., van der Schalie, R., Wagner, W. & Dorigo, W. Evolution of the ESA CCI Soil Moisture climate data records and their underlying merging methodology. *Earth System Science Data* **11**, 717–739 (2019). URL <https://essd.copernicus.org/articles/11/717/2019/>. Publisher: Copernicus GmbH. 1693
1694
1695
1696
1697
1698
1699
1700
1701
1702

[50] Preimesberger, W., Scanlon, T., Su, C.-H., Gruber, A. & Dorigo, W. Homogenization of Structural Breaks in the Global ESA CCI Soil Moisture Multisatellite 1700
1701
1702

1703 Climate Data Record. *IEEE Transactions on Geoscience and Remote Sensing*
1704 **59**, 2845–2862 (2021). URL <https://ieeexplore.ieee.org/document/9165186>.

1705

1706

1707 [51] Ashouri, H. *et al.* PERSIANN-CDR: Daily Precipitation Climate Data Record
1708 from Multisatellite Observations for Hydrological and Climate Studies. *Bul-
1709 letin of the American Meteorological Society* **96**, 69–83 (2015). URL <https:////journals.ametsoc.org/view/journals/bams/96/1/bams-d-13-00068.1.xml>. Pub-
1710 lisher: American Meteorological Society Section: Bulletin of the American
1711 Meteorological Society.

1712

1713

1714

1715

1716

1717 [52] Moesinger, L. *et al.* The global long-term microwave Vegetation Optical Depth
1718 Climate Archive (VODCA). *Earth System Science Data* **12**, 177–196 (2020).
1719 URL <https://essd.copernicus.org/articles/12/177/2020/>. Publisher: Copernicus
1720 GmbH.

1721

1722

1723

1724

1725 [53] Skulovich, O. & Gentine, P. A Long-term Consistent Artificial Intelligence and
1726 Remote Sensing-based Soil Moisture Dataset. *Scientific Data* **10**, 154 (2023).
1727 URL <https://www.nature.com/articles/s41597-023-02053-x>. Publisher: Nature
1728 Publishing Group.

1729

1730

1731

1732 [54] Boulton, C. A., Lenton, T. M. & Boers, N. Reply to: Little evidence that Ama-
1733 zonian rainforests are approaching a tipping point. *Nature Climate Change* **13**,
1734 1321–1323 (2023). Publisher: Springer Science and Business Media LLC.

1735

1736

1737

1738 [55] Tao, S. *et al.* A global long-term, high-resolution satellite radar backscatter
1739 data record (1992–2022\mathplus): merging C-band ERS/ASCAT and Ku-band
1740 QSCAT. *Earth System Science Data* **15**, 1577–1596 (2023). Publisher: Copernicus
1741 GmbH.

1742

1743

1744

1745

1746

1747

1748

[56] Bathiany, S. *et al.* Ecosystem Resilience Monitoring and Early Warning Using Earth Observation Data: Challenges and Outlook. *Surveys in Geophysics* (2024). Publisher: Springer Science and Business Media LLC. 1749
1750
1751
1752
1753
1754
1755
1756
1757
1758
1759
1760
1761
1762
1763
1764
1765
1766
1767
1768
1769
1770
1771
1772
1773
1774
1775
1776
1777
1778
1779
1780
1781
1782
1783
1784
1785
1786
1787
1788
1789
1790
1791
1792
1793
1794

[57] Lindegren, M. *et al.* Early Detection of Ecosystem Regime Shifts: A Multiple Method Evaluation for Management Application. *PLoS ONE* **7**, e38410 (2012). Publisher: Public Library of Science (PLoS). 1749
1750
1751
1752
1753
1754
1755
1756
1757
1758
1759
1760
1761
1762
1763
1764
1765
1766
1767
1768
1769
1770
1771
1772
1773
1774
1775
1776
1777
1778
1779
1780
1781
1782
1783
1784
1785
1786
1787
1788
1789
1790
1791
1792
1793
1794

[58] Dakos, V., van Nes, E. H., D'Odorico, P. & Scheffer, M. Robustness of variance and autocorrelation as indicators of critical slowing down. *Ecology* **93**, 264–271 (2012). URL <https://onlinelibrary.wiley.com/doi/abs/10.1890/11-0889.1>. _eprint: <https://onlinelibrary.wiley.com/doi/pdf/10.1890/11-0889.1>. 1749
1750
1751
1752
1753
1754
1755
1756
1757
1758
1759
1760
1761
1762
1763
1764
1765
1766
1767
1768
1769
1770
1771
1772
1773
1774
1775
1776
1777
1778
1779
1780
1781
1782
1783
1784
1785
1786
1787
1788
1789
1790
1791
1792
1793
1794

[59] Ashwin, P., Wieczorek, S., Vitolo, R. & Cox, P. Tipping points in open systems: bifurcation, noise-induced and rate-dependent examples in the climate system. *Philosophical Transactions of the Royal Society A: Mathematical, Physical and Engineering Sciences* **370**, 1166–1184 (2012). Publisher: The Royal Society. 1749
1750
1751
1752
1753
1754
1755
1756
1757
1758
1759
1760
1761
1762
1763
1764
1765
1766
1767
1768
1769
1770
1771
1772
1773
1774
1775
1776
1777
1778
1779
1780
1781
1782
1783
1784
1785
1786
1787
1788
1789
1790
1791
1792
1793
1794

[60] Guttal, V. & Jayaprakash, C. Changing skewness: an early warning signal of regime shifts in ecosystems. *Ecology Letters* **11**, 450–460 (2008). URL <https://onlinelibrary.wiley.com/doi/abs/10.1111/j.1461-0248.2008.01160.x>. _eprint: <https://onlinelibrary.wiley.com/doi/pdf/10.1111/j.1461-0248.2008.01160.x>. 1749
1750
1751
1752
1753
1754
1755
1756
1757
1758
1759
1760
1761
1762
1763
1764
1765
1766
1767
1768
1769
1770
1771
1772
1773
1774
1775
1776
1777
1778
1779
1780
1781
1782
1783
1784
1785
1786
1787
1788
1789
1790
1791
1792
1793
1794

[61] Wang, R. *et al.* Flickering gives early warning signals of a critical transition to a eutrophic lake state. *Nature* **492**, 419–422 (2012). URL <https://www.nature.com/articles/nature11655>. Publisher: Nature Publishing Group. 1749
1750
1751
1752
1753
1754
1755
1756
1757
1758
1759
1760
1761
1762
1763
1764
1765
1766
1767
1768
1769
1770
1771
1772
1773
1774
1775
1776
1777
1778
1779
1780
1781
1782
1783
1784
1785
1786
1787
1788
1789
1790
1791
1792
1793
1794

[62] Dakos, V., van Nes, E. H. & Scheffer, M. Flickering as an early warning signal. *Theoretical Ecology* **6**, 309–317 (2013). URL <https://doi.org/10.1007/s12080-013-0186-4>. 1749
1750
1751
1752
1753
1754
1755
1756
1757
1758
1759
1760
1761
1762
1763
1764
1765
1766
1767
1768
1769
1770
1771
1772
1773
1774
1775
1776
1777
1778
1779
1780
1781
1782
1783
1784
1785
1786
1787
1788
1789
1790
1791
1792
1793
1794

1795 [63] Chevalier, M. & Grenouillet, G. Global assessment of early warning signs that
1796 temperature could undergo regime shifts. *Scientific Reports* **8**, 10058 (2018).
1797 URL <https://www.nature.com/articles/s41598-018-28386-x>. Publisher: Nature
1799 Publishing Group.

1800

1801

1802 [64] Gneiting, T., Ševčíková, H. & Percival, D. B. Estimators of Fractal Dimension:
1803 Assessing the Roughness of Time Series and Spatial Data. *Statistical Science* **27**
1804 (2012). Publisher: Institute of Mathematical Statistics.

1805

1806

1807

1808 [65] Bian, J., Ma, Z., Wang, C., Huang, T. & Zeng, C. Early warning for spatial
1809 ecological system: Fractal dimension and deep learning. *Physica A: Statistical
1810 Mechanics and its Applications* **633**, 129401 (2024). Publisher: Elsevier BV.

1811

1812

1813

1814 [66] Chamberlin, T. C. Studies for Students: The Method of Multiple Working
1815 Hypotheses. *The Journal of Geology* **5**, 837–848 (1897). Publisher: University of
1816 Chicago Press.

1817

1818

1819

1820 [67] Scheffer, M., Hirota, M., Holmgren, M., Van Nes, E. H. & Chapin, F. S. Thresh-
1821 olds for boreal biome transitions. *Proceedings of the National Academy of Sciences*
1822 **109**, 21384–21389 (2012). Publisher: Proceedings of the National Academy of
1823 Sciences.

1824

1825

1826

1827 [68] Ditlevsen, P. D. & Johnsen, S. J. Tipping points: Early warning and wishful think-
1828 ing. *Geophysical Research Letters* **37** (2010). Publisher: American Geophysical
1829 Union (AGU).

1830

1831

1832

1833 [69] West, G. Scale: The Universal Laws of Growth, Innovation, Sustainability, and
1834 the Pace of Life in Organisms, Cities, Economies, and Companies: The Universal
1835 Laws of Life, Growth, and Death in Organisms, Cities, and Companies (2017).
1836

1837

1838 ISBN: 9781101621509 Num Pages: 10 Place: East Rutherford.

1839

1840

[70] Dakos, V. *et al.* Slowing down as an early warning signal for abrupt climate change. *Proceedings of the National Academy of Sciences* **105**, 14308–14312 (2008). URL <https://www.pnas.org/doi/abs/10.1073/pnas.0802430105>. Publisher: Proceedings of the National Academy of Sciences. 1841
1842
1843
1844
1845
1846
1847
1848
1849
1850
1851
1852
1853
1854
1855
1856
1857
1858
1859
1860
1861
1862
1863
1864
1865
1866
1867
1868
1869
1870
1871
1872
1873
1874
1875
1876
1877
1878
1879
1880
1881
1882
1883
1884
1885
1886

[71] Kendall, M. G. *Rank Correlation Methods* (C. Griffin, 1948). 1848
1849
1850
1851
1852
1853
1854
1855
1856
1857

[72] Sen, P. K. Estimates of the Regression Coefficient Based on Kendall’s Tau. *Journal of the American Statistical Association* **63**, 1379–1389 (1968). URL <https://www.jstor.org/stable/2285891>. Publisher: [American Statistical Association, Taylor & Francis, Ltd.]. 1851
1852
1853
1854
1855
1856
1857

[73] Conover, W. J. *Practical nonparametric statistics* (New York : Wiley, 1980). URL <http://archive.org/details/practicalnonpara0000cono>. 1858
1859
1860
1861
1862
1863
1864
1865
1866
1867

[74] Buchhorn, M. *et al.* Copernicus Global Land Cover Layers—Collection 2. *Remote Sensing* **12**, 1044 (2020). URL <https://www.mdpi.com/2072-4292/12/6/1044>. Publisher: Multidisciplinary Digital Publishing Institute. 1868
1869
1870
1871
1872
1873
1874
1875
1876
1877

[75] Siebert, S., Doll, P. & Hoogeveen, J. Development and validation of the global map of irrigation areas. *Hydrology and Earth System Sciences* (2005). 1878
1879
1880
1881
1882
1883
1884
1885
1886

[76] Zeileis, A., Leisch, F., Hornik, K. & Kleiber, C. strucchange: An R Package for Testing for Structural Change in Linear Regression Models. *Journal of Statistical Software* **7**, 1–38 (2002). URL <https://doi.org/10.18637/jss.v007.i02>. 1878
1879
1880
1881
1882
1883
1884
1885
1886

[77] Zeileis, A. A Unified Approach to Structural Change Tests Based on ML Scores, F Statistics, and OLS Residuals. *Econometric Reviews* **24**, 445–466 (2005). URL <https://doi.org/10.1080/07474930500406053>. Publisher: Taylor & Francis _eprint: <https://doi.org/10.1080/07474930500406053>. 1880
1881
1882
1883
1884
1885
1886

1887 [78] Friedman, J. H. Greedy Function Approximation: A Gradient Boosting Machine.
1888
1889 *The Annals of Statistics* **29**, 1189–1232 (2001). URL <https://www.jstor.org/stable/2699986>. Publisher: Institute of Mathematical Statistics.
1890
1891
1892
1893 [79] Roberts, D. R. *et al.* Cross-validation strategies for data with tempo-
1894 ral, spatial, hierarchical, or phylogenetic structure. *Ecography* **40**, 913–
1895 929 (2017). URL <https://onlinelibrary.wiley.com/doi/abs/10.1111/ecog.02881>.
1896 eprint: <https://nsojournals.onlinelibrary.wiley.com/doi/pdf/10.1111/ecog.02881>.
1897
1898
1899
1900 [80] Saito, T. & Rehmsmeier, M. The Precision-Recall Plot Is More Informative than
1901
1902 the ROC Plot When Evaluating Binary Classifiers on Imbalanced Datasets. *PLOS*
1903 *ONE* **10**, e0118432 (2015). URL <https://journals.plos.org/plosone/article?id=10.1371/journal.pone.0118432>. Publisher: Public Library of Science.
1904
1905
1906
1907
1908 [81] Lundberg, S. M. & Lee, S.-I. A Unified Approach to Interpreting Model Pre-
1909 dictions. *NIPS’17: Proceedings of the 31st International Conference on Neural*
1910
1911 *Information Processing Systems* (2017).
1912
1913
1914 [82] Cohen, J. A Coefficient of Agreement for Nominal Scales. *Educational and*
1915 *Psychological Measurement* **20**, 37–46 (1960). URL <https://doi.org/10.1177/001316446002000104>. Publisher: SAGE Publications Inc.
1916
1917
1918
1919 [83] Light, R. J. Measures of response agreement for qualitative data: Some
1920 generalizations and alternatives. *Psychological Bulletin* **76**, 365–377 (1971).
1921
1922
1923
1924 [84] Singer, M. B. *et al.* Hourly potential evapotranspiration at 0.1° resolution for the
1925 global land surface from 1981-present. *Scientific Data* **8**, 224 (2021). URL <https://www.nature.com/articles/s41597-021-01003-9>. Publisher: Nature Publishing
1926
1927
1928
1929
1930
1931
1932 Group.

[85] Fan, Y., Li, H. & Miguez-Macho, G. Global Patterns of Groundwater Table Depth. *Science* **339**, 940–943 (2013). URL <https://www.science.org/doi/10.1126/science.1229881>. Publisher: American Association for the Advancement of Science.

1933
1934
1935
1936
1937
1938
1939
1940
1941
1942
1943
1944
1945
1946
1947
1948
1949
1950
1951
1952
1953
1954
1955
1956
1957
1958
1959
1960
1961
1962
1963
1964
1965
1966
1967
1968
1969
1970
1971
1972
1973
1974
1975
1976
1977
1978

Table of Contents

Table S1 Sensitivity EWS calculation parameters	2
Figure S2 Kendall's τ of individual EWS indicators for transpiration.....	3
Figure S2 Kendall's τ of individual EWS indicators for soil moisture	4
Figure S2 Kendall's τ of individual EWS indicators for precipitation	5
Figure S3 Delta of individual EWS indicators for transpiration.....	6
Figure S3 Delta of individual EWS indicators for soil moisture	7
Figure S3 Delta of individual EWS indicators for precipitation	8
Figure S4 Theil-Sen slope of individual EWS indicators for transpiration.....	9
Figure S4 Theil-Sen slope of individual EWS indicators for soil moisture.....	10
Figure S4 Theil-Sen slope of individual EWS indicators for precipitation	11
Figure S5 Change in mean of individual EWS indicators for transpiration	12
Figure S5 Change in mean of individual EWS indicators for soil moisture.....	13
Figure S5 Change in mean of individual EWS indicators for precipitation	14
Figure S6 Agreement across trend estimation methods	15
Figure S7 Cumulative land area with detected breakpoints.....	16
Figure S8 F1 score of abrupt shift detection methods	17
Table S9 Environmental feature variables included in XGBoost models.....	18
Table S10 Class distribution and model performance.....	19
Figure S11 PR and ROC curves of trained XGBoost models	20
Figure S12 Global variable importances	21
Figure S13 Partial dependence plots of top 5 variables.....	22
Figure S14 Biome-resolved absolute SHAP values	23

Table S1 Sensitivity EWS calculation parameters

Table S1. Sensitivity of transpiration, soil moisture, and precipitation EWS signs to analysis configuration for a 50 by 50-pixel tile at 0.25 degrees. Values are Cohen's K (chance-corrected agreement) computed pixel-wise between class-labelled Kendall's τ maps (-1, 0, +1), where $|\tau| < 0.05$ and $p > 0.05$ are treated as 0. Light's K is the pairwise-average K across all configuration pairs. Columns report the mean K across matched configuration pairs that differ only in sampling frequency (weekly vs monthly), window length (2.5-, 5-, 10-years), first-differencing, or STL robustness choice. Negative values indicate systematic disagreement beyond chance.

Variable	Indicator	Light's K	Frequency only	Window only	Diff. only	STL only
Transpiration	AC1	0.157	0.036	0.417	0.272	0.523
	SD	0.096	-0.111	0.354	0.406	0.329
	Skew	0.067	0.132	0.482	-0.195	0.548
	Kurt	0.106	-0.045	0.289	0.279	0.556
	FD	0.153	-0.080	0.472	0.415	0.240
	Mean	0.116	-0.014	0.403	0.235	0.439
Soil moisture	AC1	0.174	0.444	0.231	0.156	0.508
	SD	0.558	0.643	0.631	0.705	0.514
	Skew	0.035	0.004	0.391	-0.032	0.171
	Kurt	0.211	0.325	0.422	0.111	0.213
	FD	0.184	0.176	0.760	0.058	0.638
	Mean	0.233	0.318	0.487	0.200	0.409
Precipitation	AC1	0.206	0.027	0.521	0.369	0.596
	SD	0.291	0.169	0.580	0.433	0.623
	Skew	0.092	0.030	0.526	-0.027	0.432
	Kurt	0.164	0.027	0.483	0.330	0.483
	FD	0.199	0.027	0.497	0.288	0.503
	Mean	0.190	0.056	0.521	0.278	0.527

Figure S2 Kendall's τ of individual EWS indicators for transpiration

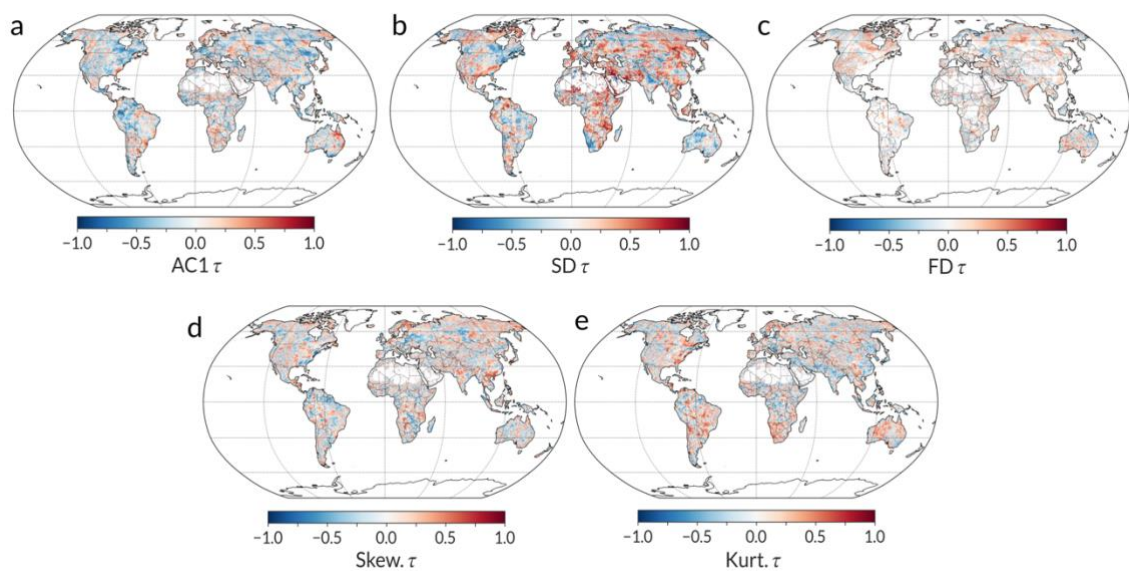


Figure S2a. Transpiration. Kendall's τ of individual EWS indicators. No significance filtering is applied.

Figure S2 Kendall's τ of individual EWS indicators for soil moisture

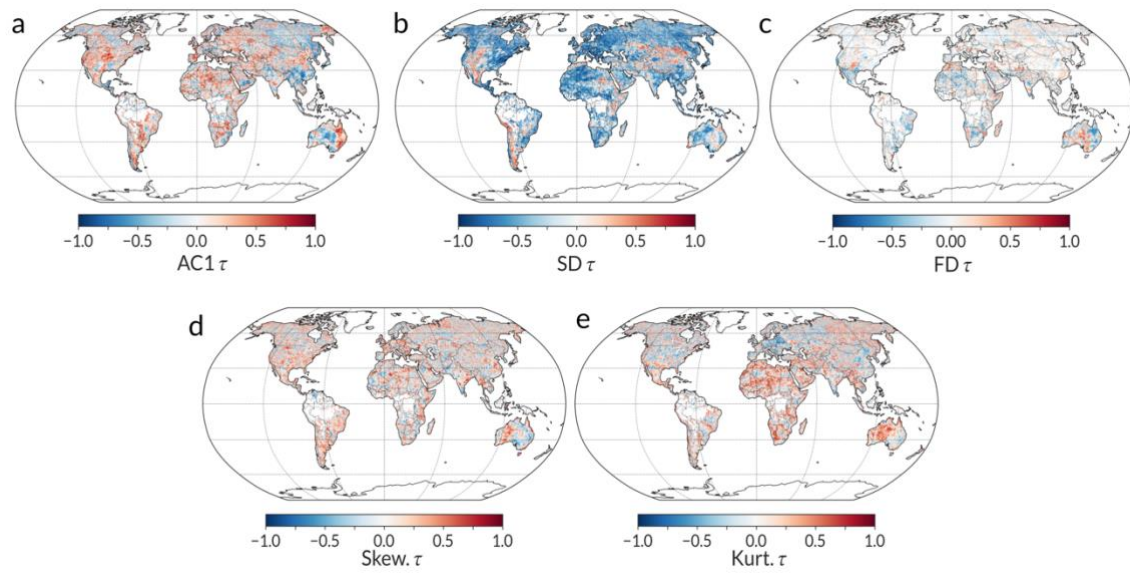


Figure S2b. Soil moisture. Kendall's τ of individual EWS indicators. No significance filtering is applied.

Figure S2 Kendall's τ of individual EWS indicators for precipitation

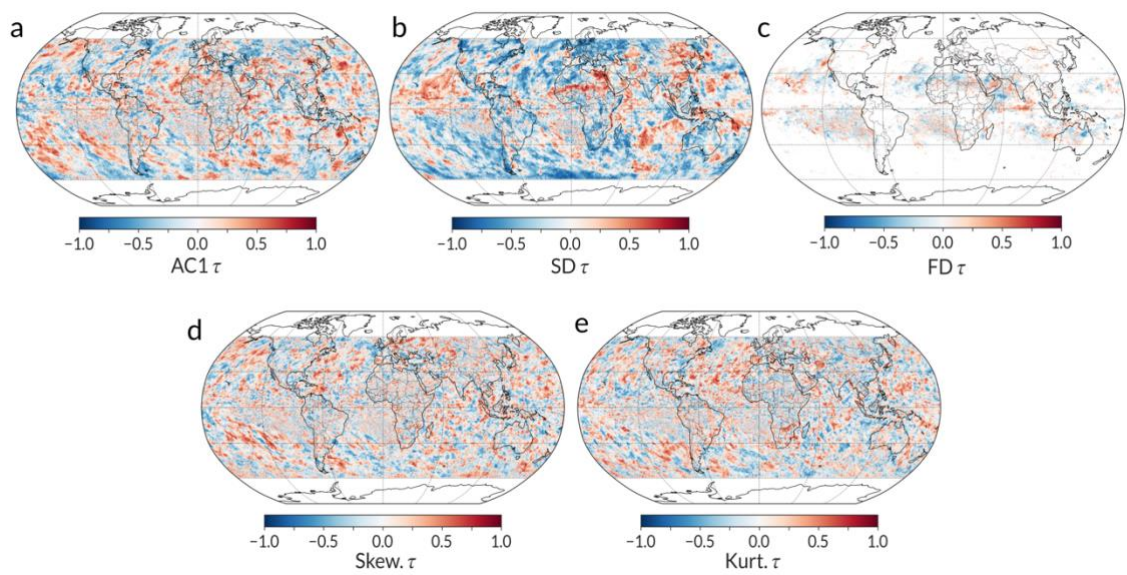


Figure S2c. Precipitation. Kendall's τ of individual EWS indicators. No significance filtering is applied, and Kendall's τ of ocean pixels are included.

Figure S3 Delta of individual EWS indicators for transpiration

Here, we calculated the time-ordered difference between the minimum and maximum value of the each of the EWS indicators (δ) over the time series (as per Rocha, 2022), which provides information about the absolute change in indicator value over the time series.

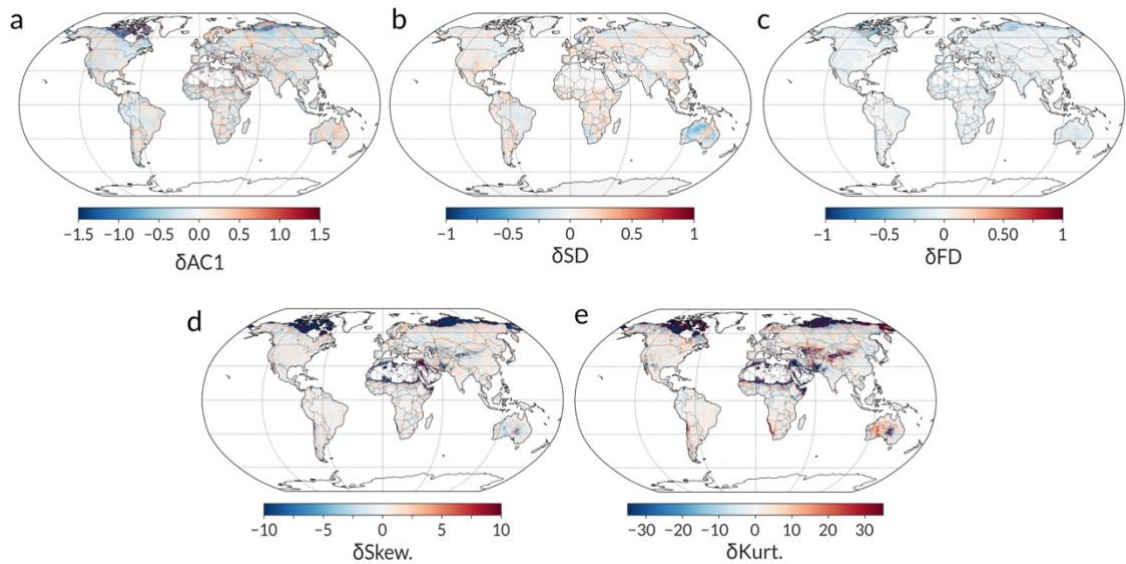


Figure S3a. Transpiration. Time ordered difference between the minimum and maximum value of the EWS indicators. No significance filtering is applied.

Figure S3 Delta of individual EWS indicators for soil moisture

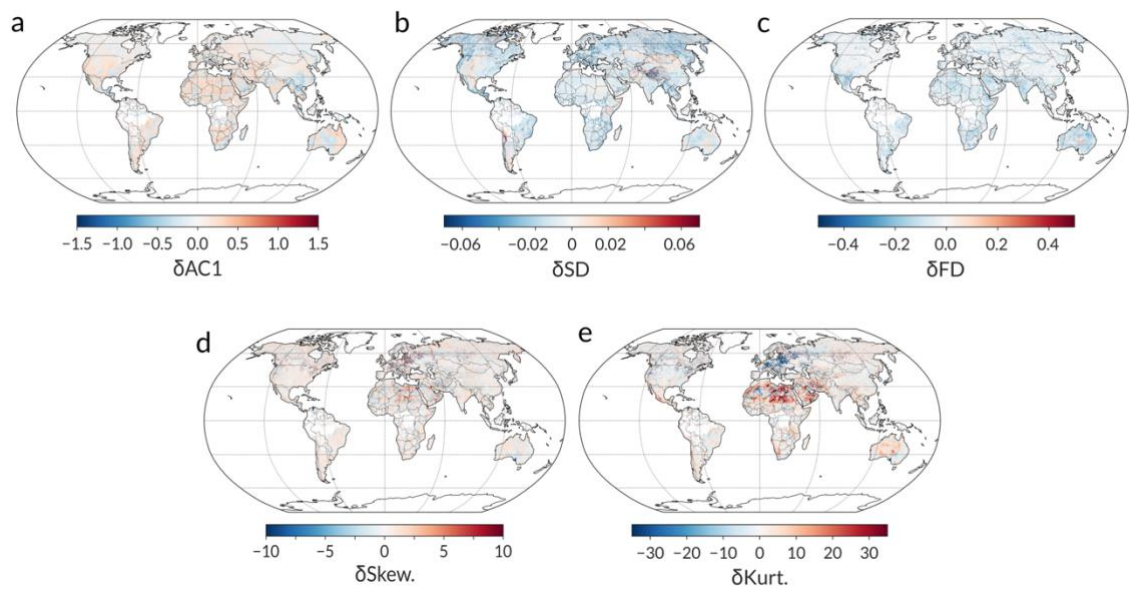


Figure S3b. Soil moisture. Time ordered difference between the minimum and maximum value of the EWS indicators. No significance filtering is applied.

Figure S3 Delta of individual EWS indicators for precipitation

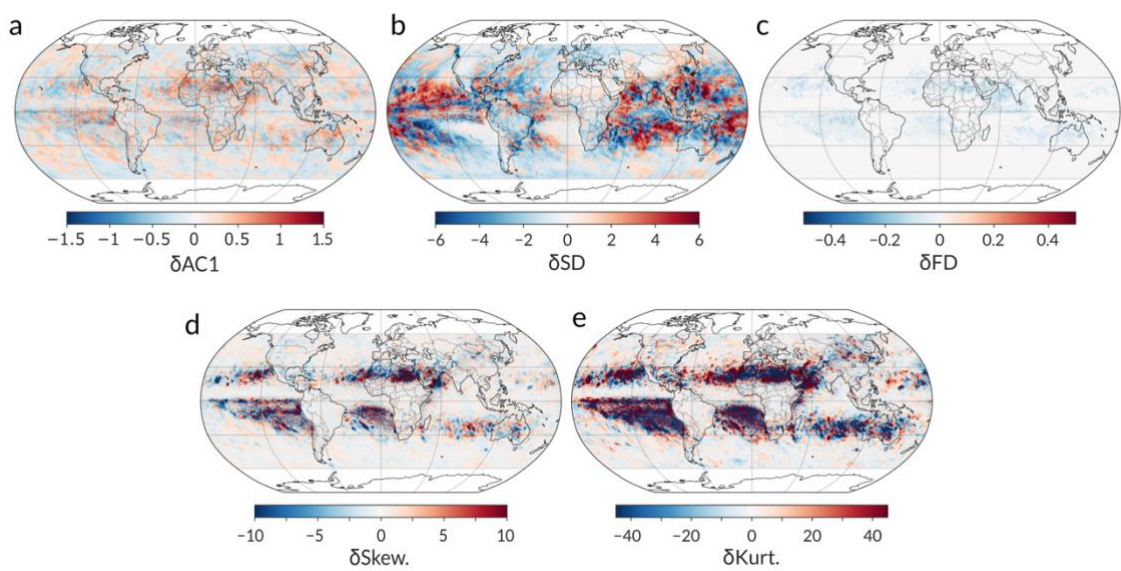


Figure S3c. Precipitation. Time ordered difference between the minimum and maximum value of the EWS indicators. No significance filtering is applied, and δ of ocean pixels are included.

Figure S4 Theil-Sen slope of individual EWS indicators for transpiration

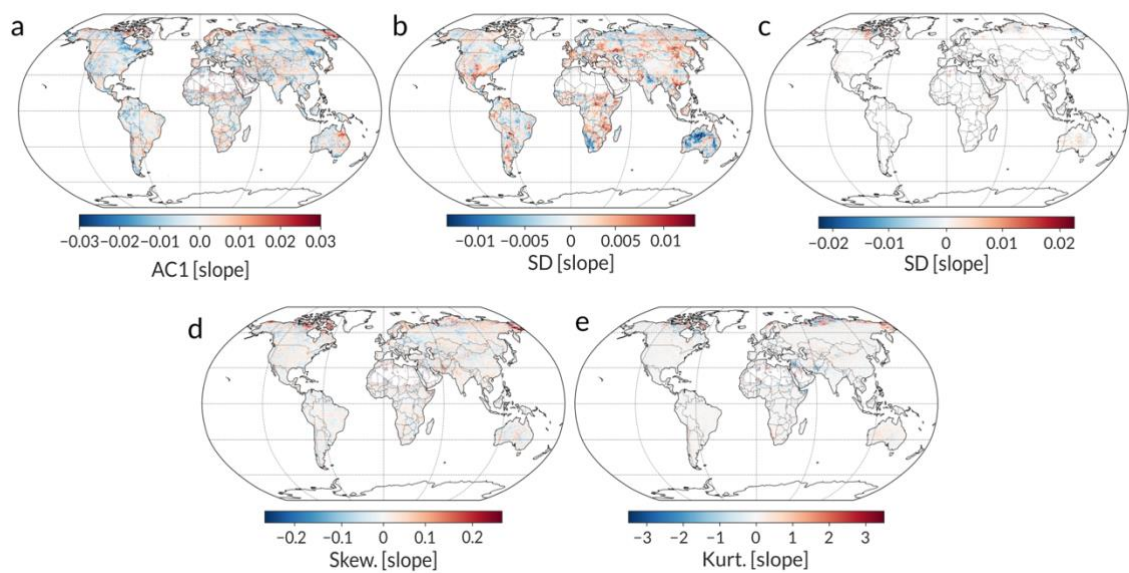


Figure S4a. Transpiration. Theil-Sen slope of the EWS indicators. No significance filtering is applied.

Figure S4 Theil-Sen slope of individual EWS indicators for soil moisture

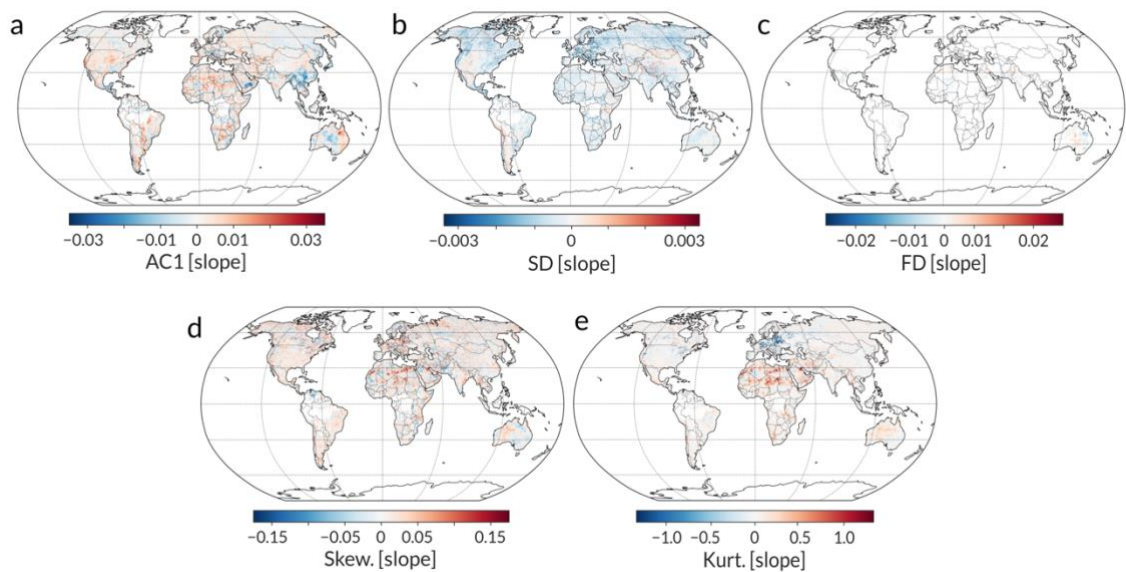


Figure S4b. Soil moisture. Theil-Sen slope of the EWS indicators. No significance filtering is applied.

Figure S4 Theil-Sen slope of individual EWS indicators for precipitation

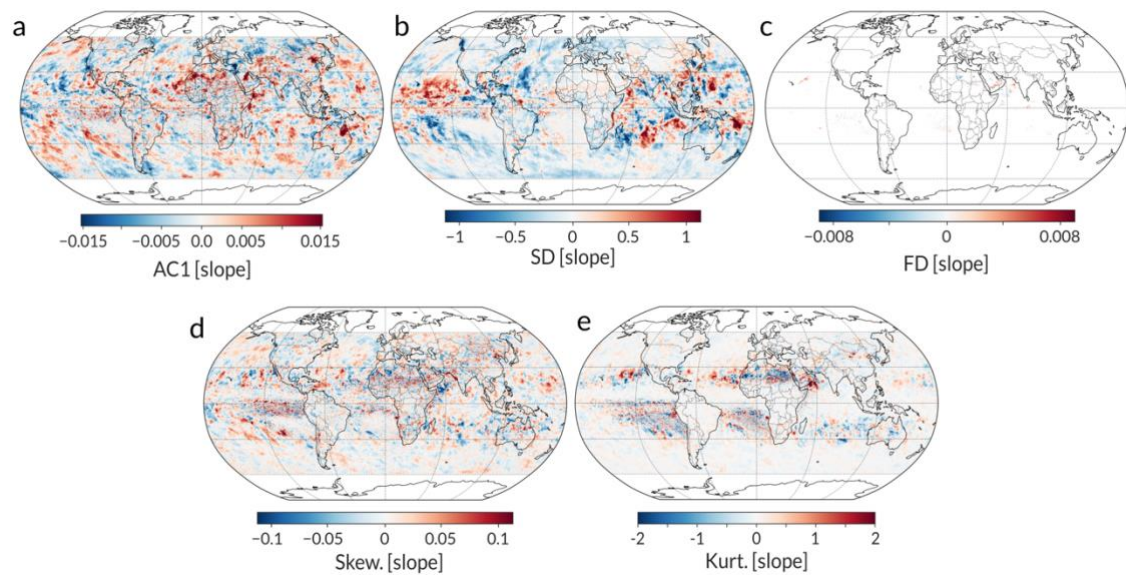


Figure S4c. Precipitation. Theil-Sen slope of the EWS indicators. No significance filtering is applied, and Theil-Sen slopes of ocean pixels are included.

Figure S5 Change in mean of individual EWS indicators for transpiration

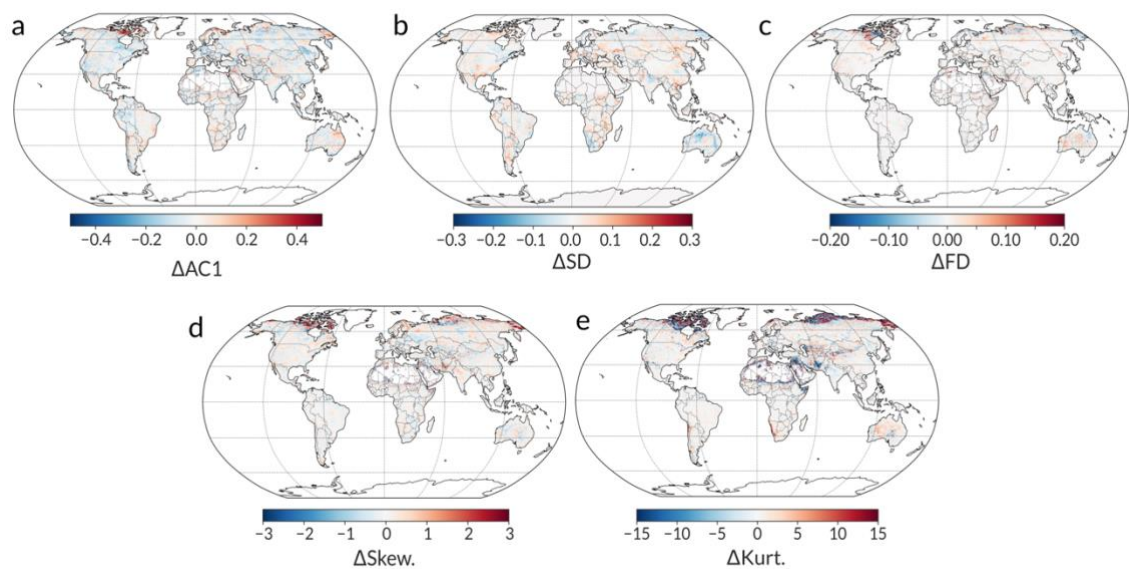


Figure S5a. Transpiration. Difference between the means of the EWS indicator value in the second half and the first half of the indicator time series.

Figure S5 Change in mean of individual EWS indicators for soil moisture

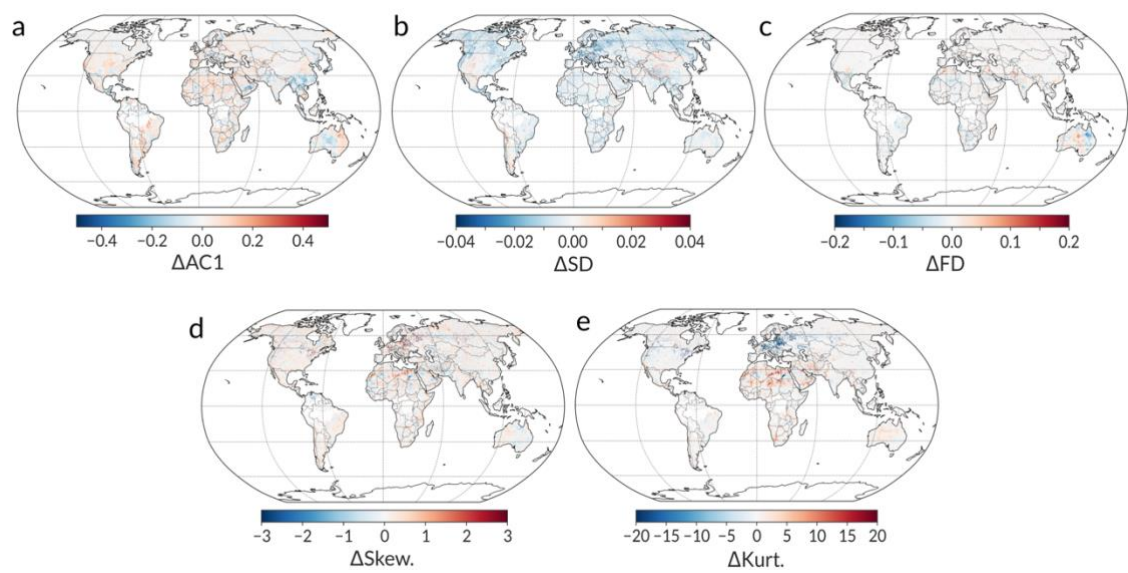


Figure S5b. Soil moisture. Difference between the means of the EWS indicator value in the second half and the first half of the indicator time series.

Figure S5 Change in mean of individual EWS indicators for precipitation

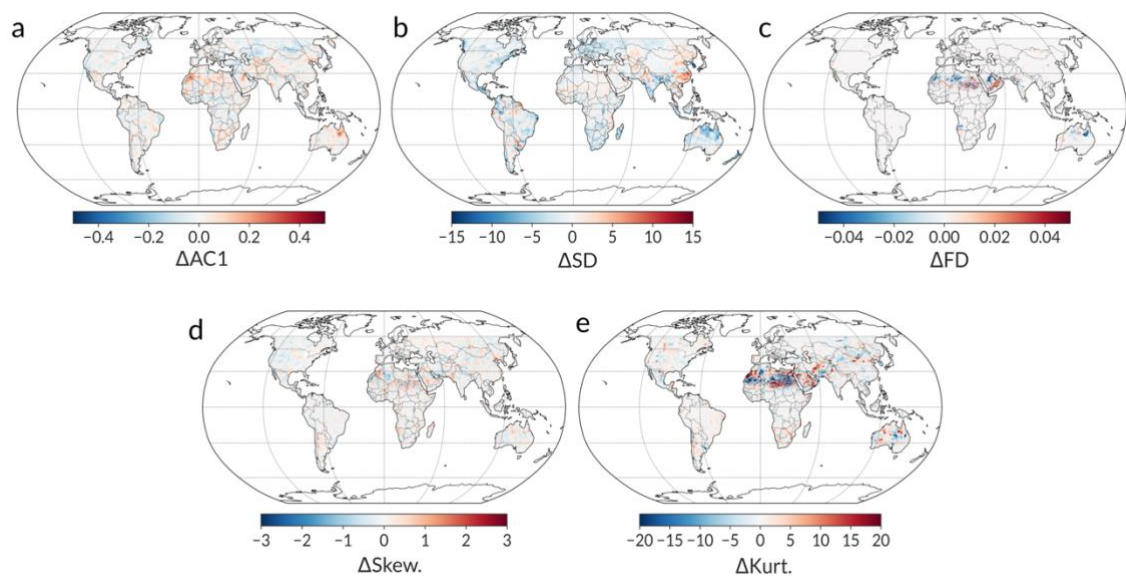


Figure S5c. Precipitation. Difference between the means of the EWS indicator value in the second half and the first half of the indicator time series.

Figure S6 Agreement across trend estimation methods

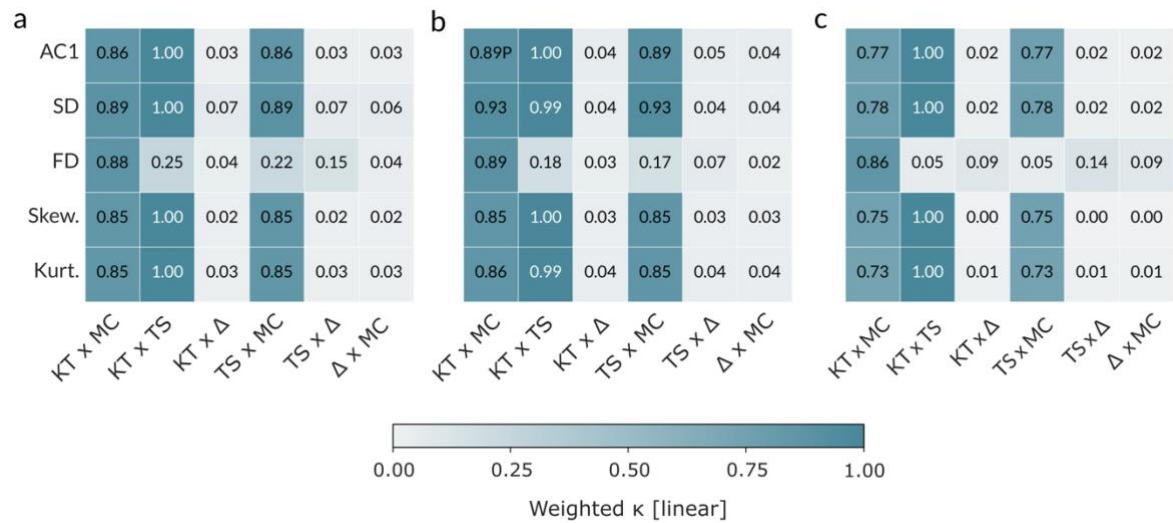


Figure S6. Agreement between methods of trend detection. Comparison of trend estimation approaches for AC1, SD, FD, Skew., and Kurt. between KT (Kendall-Tau, $p < 0.05$), TS (Theil-Sen slope, $p < 0.05$), Δ (time-ordered difference between maximum and minimum), and MC (mean-change between time series halves, Welch's t -test $p < 0.05$) using all grid cells ($n = 1036800$). Heatmap's report the linear-weighted Cohen's κ across method pairs for each indicator.

Figure S7 Cumulative land area with detected breakpoints

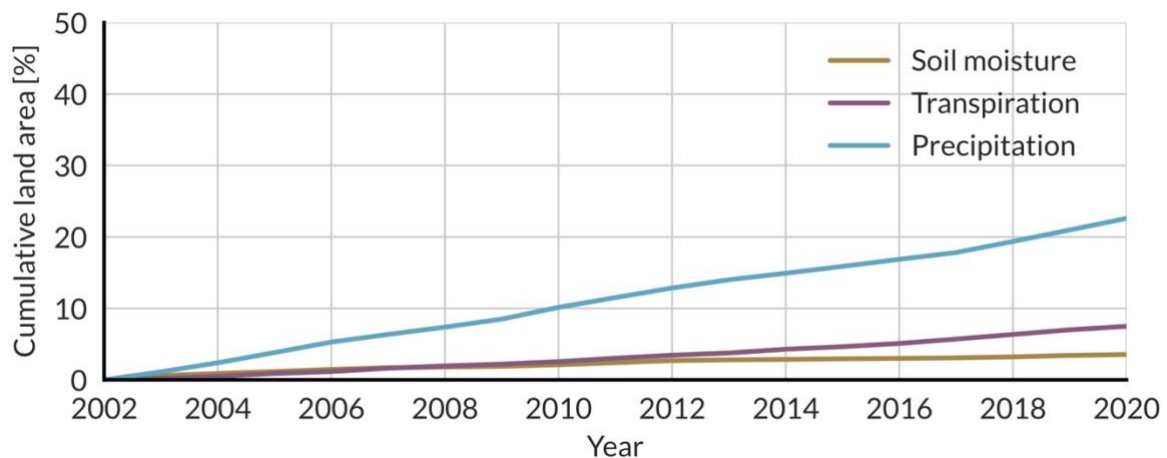


Figure S7. Cumulative land area with breakpoints detected using the structural change test ($p < 0.05$). The total land area for precipitation is 60°S to 60°N .

Figure S8 F1 score of abrupt shift detection methods

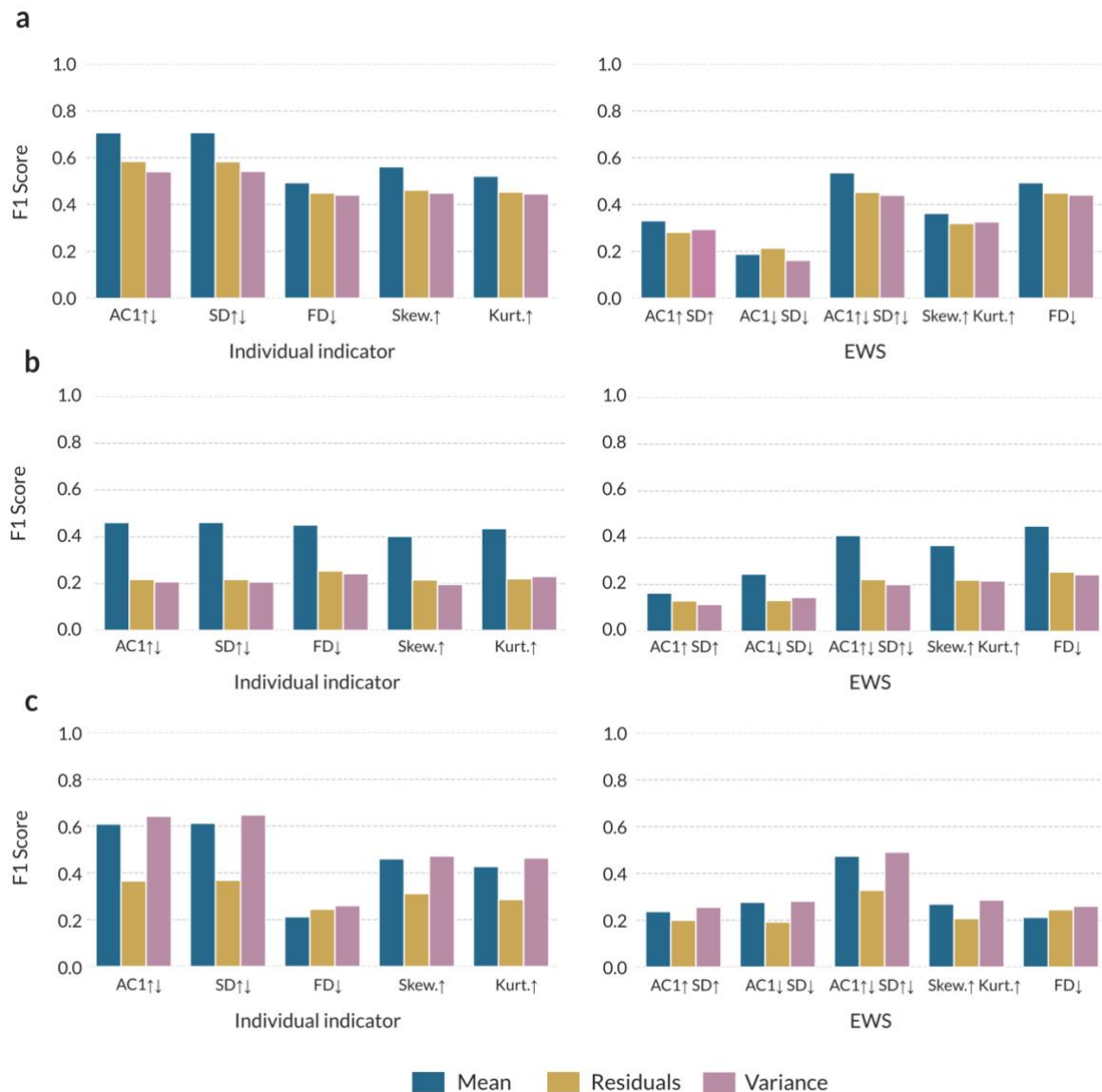


Figure S10. F1 score of the different abrupt shift methods. Calculated from the confusion matrix that compares Kendall's τ from the full time series of the green water variable to pixels where we detect an abrupt shift, for transpiration (a), soil moisture (b), and precipitation (c). We use the detected breakpoints in residuals as the most conservative test to reduce false positives.

Table S9 Environmental feature variables included in XGBoost models

Table S9. Environmental feature variables for XGBoost classification model. The data sources, green water variable for which the features were included, and processing notes are listed.

Driver	Source	Time	Target	Processing notes
Temperature	ERA5 monthly	2000-2023	P, Et, SM	Calculated mean, SD, and trend of monthly values over time.
Precipitation	ERA5 monthly	2000-2023	P, Et, SM	Calculated mean, SD, and trend of monthly values over time.
Soil moisture	ERA5 monthly	2000-2023	P, Et, SM	Calculated mean, SD, and trend of monthly values over time.
Transpiration	ERA5 Land	2000-2023	P, Et, SM	Calculated mean, SD, and trend of monthly values over time.
Potential evapo-transpiration [Epot]		2000-2023	P, Et, SM	Coarsened to 0.25 degrees, resampled to monthly. Calculated mean, SD, and trend of monthly values over time.
ENSO	NASA	2000-2023	P, Et, SM	Re-indexed ENSO index to precipitation time indices, and calculated the pixel-wise correlation between ENSO and precipitation.
Groundwater table depth [GW]		2000-2023	Et, SM	Coarsened to 0.25 degrees, calculated mean, SD, and trend of monthly values over time.
Boundary layer height	ERA5 Monthly	2000-2023	P, Et, SM	Calculated mean, SD, and trend of monthly values over time.
Convective available potential energy [CAPE]	ERA5 monthly	2000-2023	P, Et, SM	Calculated mean, SD, and trend of monthly values over time.
Gross Primary Productivity [GPP]	MODIS	2014-2023	Et, SM	Calculated mean, SD, and trend of monthly values over time. NaN values (i.e. no vegetation) filled with 0.
Tree cover	ERA5 Land	2000-2023	Et, SM	Calculated mean, SD, and trend of monthly values over time. NaN values (i.e. no vegetation) filled with 0.
Non-tree cover	ERA5 Land	2000-2023	Et, SM	Calculated mean, SD, and trend of monthly values over time. NaN values (i.e. no vegetation) filled with 0.
Irrigated area	FAO	2005	Et, SM	Percentage area equipped for irrigation, NaN values (i.e. no irrigation) filled with 0.

Table S10 Class distribution and model performance

The XGBoost classifier was trained with the following hyperparameters: 300 trees, maximum depth = 8, learning regularization parameters $\lambda = 5$, $\alpha = 0.1$, and subsampling = 0.8). Models were trained on EWS and driver predictors simultaneously. We assess performance was assessed using out-of-fold predictions and cross-validation models, aggregated across folds. We report threshold-agnostic metrics, and use area under the precision–recall curve (PR-AUC) as the primary score, which is able to handle class-imbalance. Fold-specific metrics were summarized by mean and standard deviation.

Table S10. Class distribution and model performance across folds for XGBoost classifier models for green water variables.

Variable	N samples	N positives	N folds	Positives per fold	PR AUC [mean \pm SD]	ROC AUC [mean \pm SD]	Baseline AP	AP increase	Normalised AP increase
Transpiration	234460	1490	5	2981	0.494 \pm 0.039	0.903 \pm 0.012	0.064	7.719	0.459
Soil moisture	205411	2707	5	541.4	0.215 \pm 0.040	0.931 \pm 0.008	0.013	16.54	0.205
Precipitation	177810	8241	5	1648.2	0.330 \pm 0.042	0.834 \pm 0.013	0.046	7.152	0.29

Figure S11 PR and ROC curves of trained XGBoost models

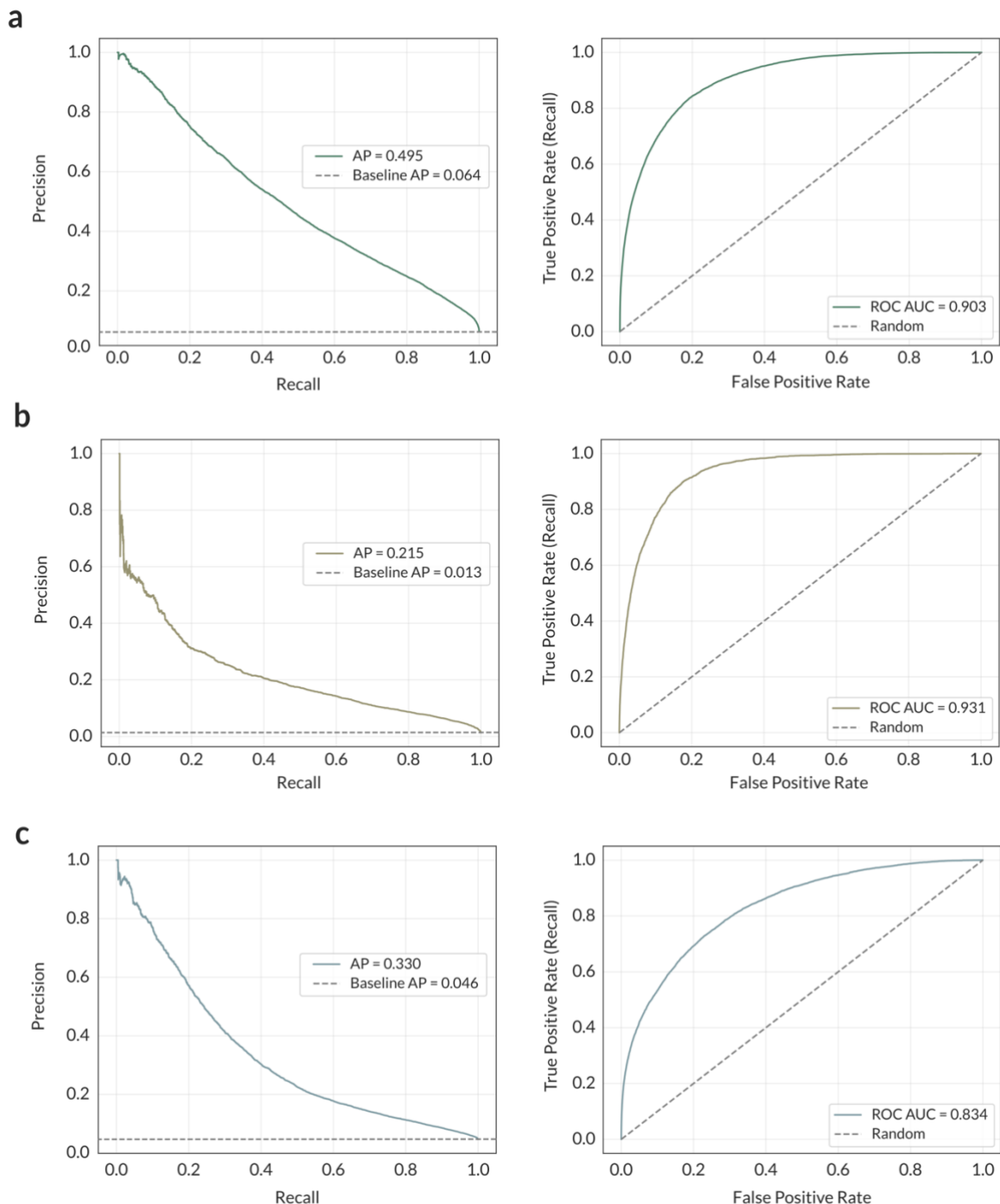


Figure S11. PR and ROC curves for trained XGBoost models for transpiration (a), soil moisture (b) and precipitation (c), from which performance metrics were calculated.

Figure S12 Global variable importances

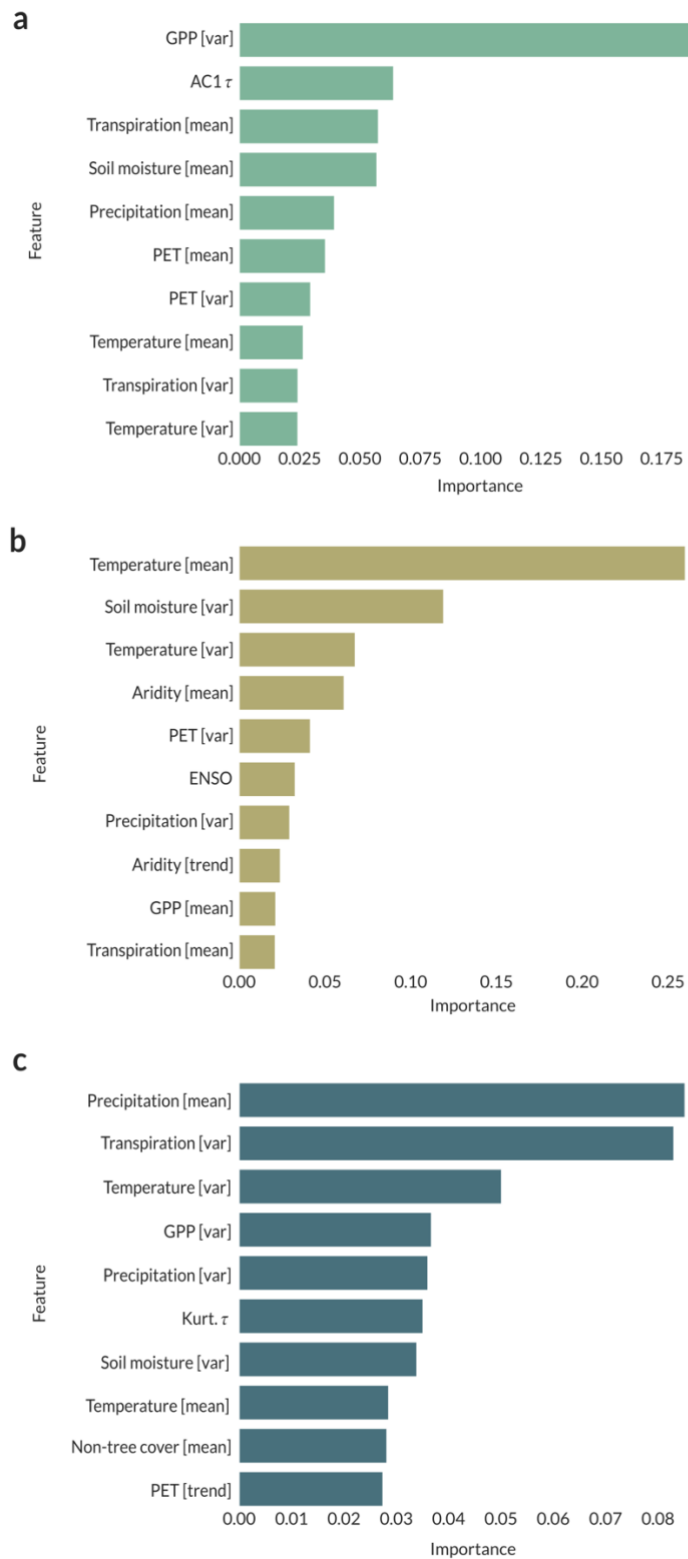


Figure S12. Global variable importances for transpiration (a), soil moisture (b) and precipitation (c).

Figure S13 Partial dependence plots of top 5 variables

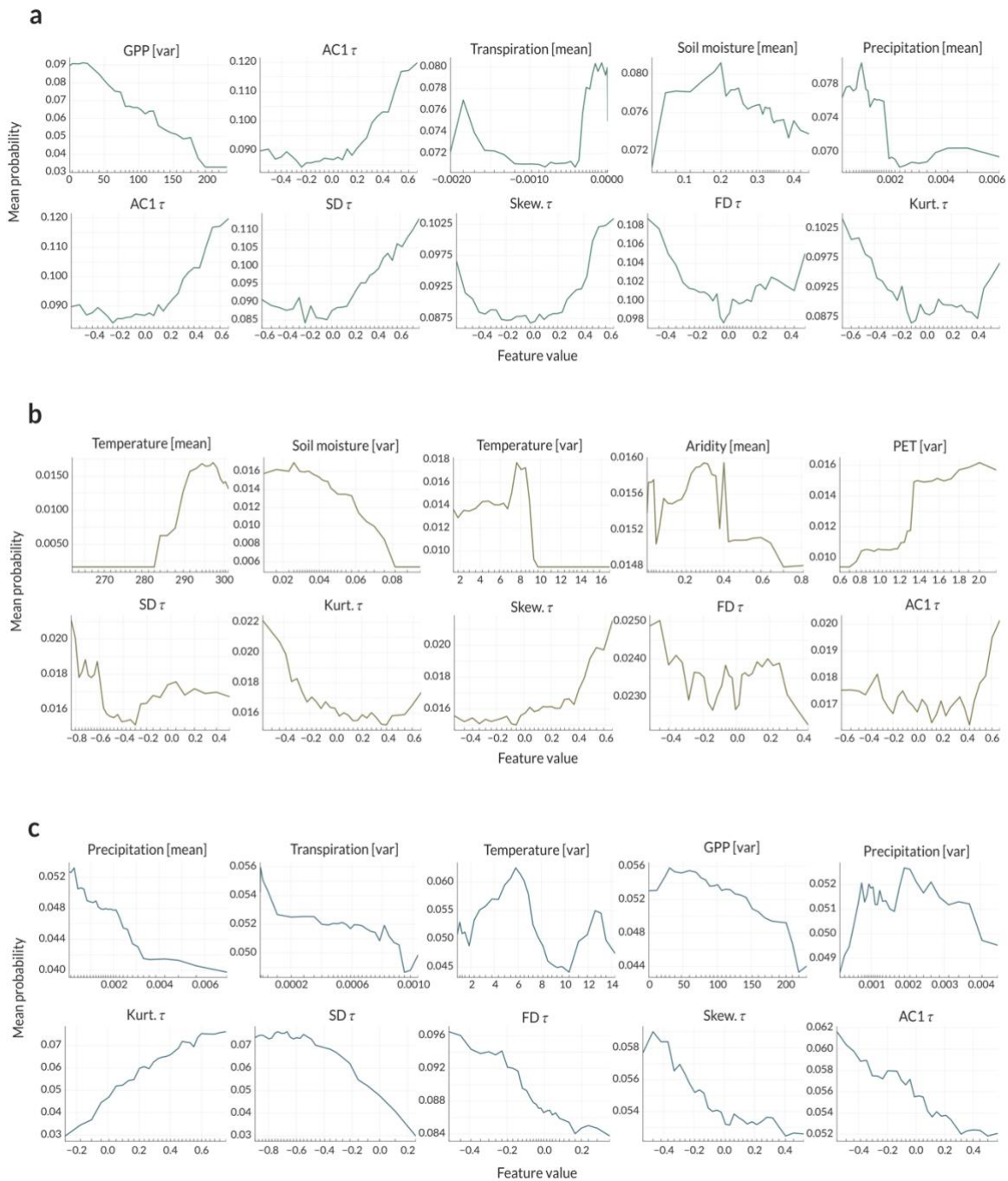


Figure S13. Partial Dependence Plots for top five variables sorted by variable importance (top panel), and for EWS τ 's, sorted by variable importance (lower panel), for transpiration (a), soil moisture (b) and precipitation (c).

Figure S14 Biome-resolved absolute SHAP values

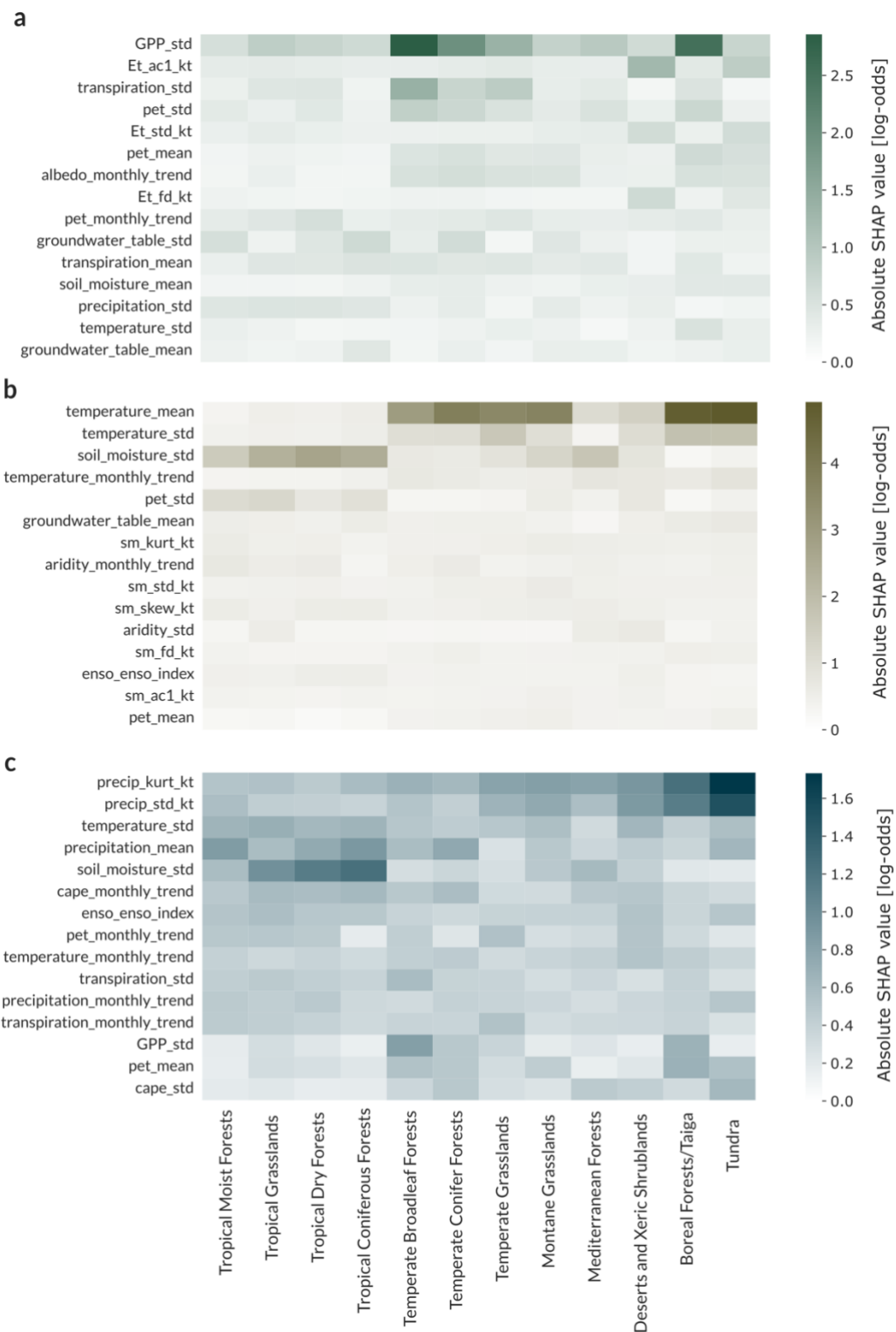


Figure S14. Biome-resolved absolute SHAP values for transpiration (a), soil moisture (b) and precipitation (c).